

Low-Tropospheric Shear in the Structure of Squall Lines: Impacts on Latent Heating under Layer-Lifting Ascent

DIEGO A. ALFARO

Universidad Nacional Autónoma de México, Mexico City, Mexico

(Manuscript received 2 June 2016, in final form 1 October 2016)

ABSTRACT

This study analyzes the dependence of the intensity of simulated midlatitude squall lines (SLs) at maturity on the strength of the environmental low-tropospheric shear, focusing on the amplitude of the latent heating produced within the deep convective region. The hypothesis motivating this investigation is that shear fundamentally affects system strength by modulating the mean convective instability of the storm-relative inflowing air, which is justified by the layer-lifting nature of convection in SLs.

The layer-lifting model of convection (LLMC) is proposed for measuring convective instability in the context of SLs, wherein latent heating is estimated by contemplating the storm-relative inflow of CAPE. This framework is used for defining LLMC indices for the precipitation rate and the updraft's strength and verticality. Idealized SLs at maturity, simulated in a variety of kinematic and thermodynamic environments, encompass wide-ranging values of LLMC indices and degrees of cold pool–shear balance within the spectrum of cold pool–dominated storms.

LLMC indices account for much of the intercase variability in the updraft's strength and verticality, the precipitation rate, and the convective mode apparent in radar reflectivity plots. It is found that the low-tropospheric shear fundamentally affects the intensity of SLs through its effects on latent heating, with stronger shear leading to larger inflowing convectively unstable air as a fraction of the total storm-relative inflow, favoring system intensity. This behavior could largely explain the dependence of storm intensity on the strength of shear documented in previous investigations, as cold pool–shear balance appears to be less restrictive on the intensity of mature SLs than the strength of the shear alone.

1. Introduction

Mesoscale convective systems are frequently organized with a nearly continuous line of deep convection, both in the tropics (Rickenbach and Rutledge 1998; LeMone et al. 1998) and in midlatitudes (Parker and Johnson 2000). Such storms, referred to as squall lines (SLs), can sustain long-lasting deep convective motions in the absence of mesoscale forcing—a property termed by LeMone et al. (1998) as self-organization. It is well known that the self-organization of SLs requires an environmental flow with significant convective instability (e.g., Alfaro and Khairoutdinov 2015, hereafter AK) and vertical wind shear (e.g., Rotunno et al. 1988, hereafter RKW88). The purpose of this study is to investigate how the environmental low-tropospheric shear affects the structure and intensity of severe midlatitude SLs, focusing on the impacts of the strength

of shear on the latent heating produced within the deep convective region of mature storms.

The association between the organization of SLs and the line-perpendicular component of the shear vector has been recognized at least since the seminal work of Newton (1950). Newton argues that SLs derive kinetic energy from the environment to propagate ahead of their parent cold front. It was not until the advent of numerical modeling of atmospheric deep convection that the portion of the environmental shear in the lower troposphere was recognized as a key element modulating the morphology of SLs. Hane (1973) and Thorpe et al. (1982), who performed two-dimensional simulations of midlatitude SLs, were the first to recognize the importance that low-tropospheric shear exerts on the organization and intensity of SLs. The latter study suggests that surface-based shear can favor prolonged and intense storms by enabling the edge of the outflow produced by precipitation (also referred to as a cold pool) to remain aligned with previously triggered deep convective cells.

Corresponding author e-mail: Diego Alfaro, diego.alfaro@atmosfera.unam.mx

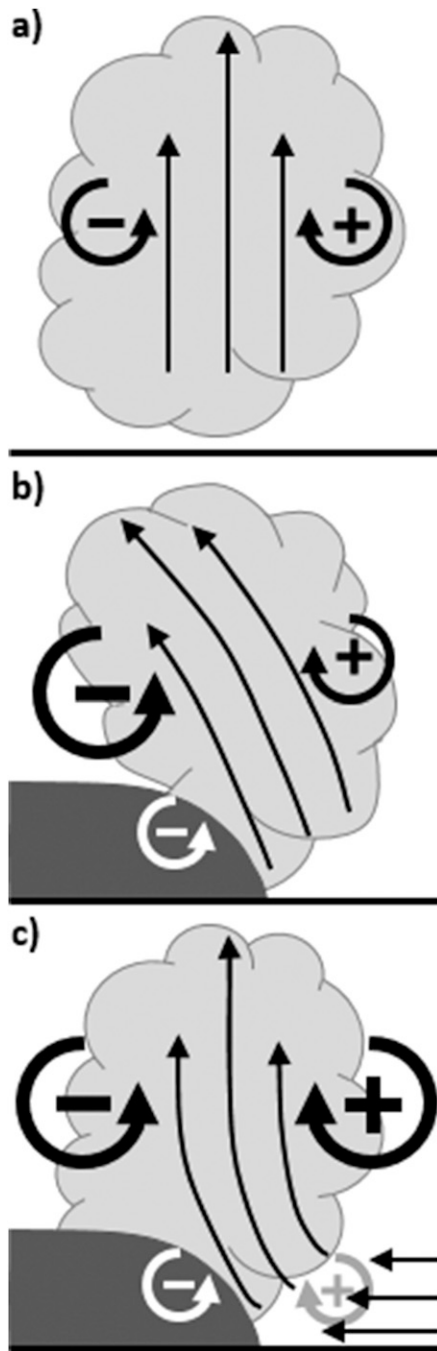


FIG. 1. Schematic diagrams showing two-dimensional updrafts and their associated horizontal vorticity distributions (round arrows). (a) The updraft is horizontally symmetric, with a vorticity dipole around the maximum vertical wind speed resulting from positive buoyancy. Latent heating is assumed to be the only source of vorticity. (b) The updraft is triggered by a cold pool in an un-sheared environment, such that the vorticity generated at the outflow's edge breaks the symmetry assumed to hold in (a), causing the updraft to tilt over the cold pool. (c) The updraft is triggered by a cold pool in an environment with low-tropospheric shear. The vorticity of the environmental shear has opposite sign to that of the vorticity generated at the outflow's edge, tending to restore the updraft's symmetry and leading to more vertical and deeper-reaching ascent.

A different interpretation was proposed by RKW88, which emphasizes vorticity dynamics on the plane perpendicular to the deep convective line (Fig. 1). RKW88 argue that a cold pool, which baroclinically generates horizontal vorticity at its edge, induces a circulation that tends to sweep surface-based parcels over and behind the outflow's edge, leading to slanted updrafts. According to RKW88, shear can counter the circulation induced by the cold pool if the sign of the environmental vorticity in the lower troposphere is opposite to the vorticity generated at the cold pool's edge. In this view, the environmental shear tends to produce downshear slanted updrafts while, on the other hand, the cold pool tends to produce upshear-leaning updrafts. Therefore, the orientation, verticality, and vigor of ascent of surface-based parcels depend on the magnitude of the low-tropospheric shear relative to the rate of vorticity generation at the cold pool's edge, with an optimal state of intense, vertical, and deep-reaching updrafts achieved when the shear balances the cold pool-induced circulation. This conceptual framework of cold pool-shear balance is commonly referred to as RKW theory.

RKW theory has been corroborated repeatedly in idealized SL simulations (e.g., Weisman et al. 1988; Weisman and Rotunno 2004, hereafter WR04; Bryan et al. 2006, hereafter BKP06), leading to wide-ranging acceptance of the vorticity balance framework, notwithstanding an extensive literature questioning the applicability of RKW theory to real-world SLs (see the review in WR04; Stensrud et al. 2005, hereafter SCDE05; Coniglio et al. 2012). Of particular relevance to this study is AK's contention that previous studies supporting RKW theory might have partly misattributed systematic variations in SL intensity to vorticity balance, particularly those features arising from the dependence of latent heating on the strength of the shear. More specifically, storms simulated by AK in environments with stronger low-tropospheric shear, for a given thermodynamic sounding, produce greater inflow of convectively unstable air as a fraction of the total storm-relative inflow. Such fraction, AK argue, modulates the latent heating produced under the highly turbulent layer-lifting ascent that occurs within the deep convective region of SLs (e.g., Zipser 1977; Bryan and Fritsch 2000; AK). It follows that the shear's strength can affect frequently used metrics of system intensity (e.g., maximum vertical wind speed and precipitation rates) by means that are not contemplated conceptually by RKW theory.

Motivated by AK's study, our main interest is to determine the extent to which latent heating under layer-lifting ascent can explain the dependence of the

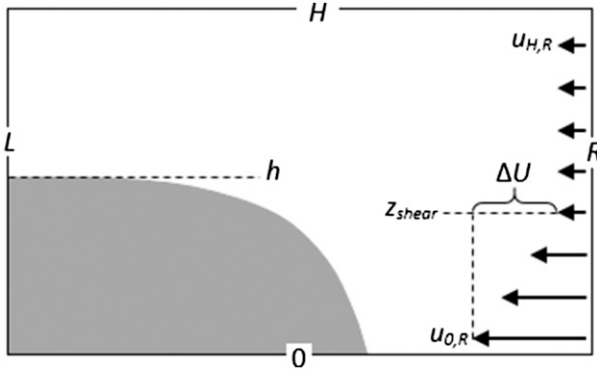


FIG. 2. Schematic depiction of a two-fluid density current flow. The gray area represents the denser fluid. See text for more details.

intensity of SLs on the low-tropospheric shear, focusing on storms that develop intense cold pools. We proceed by elaborating the layer-lifting model of convection (LLMC), a framework that contemplates system-relative fluxes of relevant parameters throughout the troposphere, allowing the formulation of a metric of convective instability that incorporates the aforementioned effects of shear. This metric is used for defining layer-lifting indices for the precipitation rate, the updraft's strength, and the updraft's slope, which are tested for their diagnostic skill in relation to idealized SLs simulated in various kinematic and thermodynamic environments. Such analyses constitute the primary means for evaluating the merit of the LLMC and the extent to which shear affects SL intensity by modulating latent heating in the deep convective region.

The layout of this paper is as follows. [Section 2](#) encompasses relevant background material, including a review of RKW theory, which will be referred to repeatedly throughout the text, followed by a description of the LLMC and the formulation of layer-lifting indices. [Section 3](#) describes the methodology, specifying the numerical framework and environments to be considered. [Section 4](#) presents results of the simulated SLs, which focus on the performance of layer-lifting indices as diagnostics of the intensity and structure of the storms. In view of such results, [section 5](#) discusses the LLMC and implications for the application of RKW theory to SLs, followed by conclusions in [section 6](#).

2. Background

a. RKW theory

The main ideas underlying RKW theory can be conveyed by a two-dimensional flow on a plane perpendicular to the deep convective line. Following [RKW88](#),

we consider the vorticity equation for an inviscid Boussinesq fluid

$$\bar{\rho} \frac{d}{dt} \frac{\eta}{\bar{\rho}} = \frac{-\partial b}{\partial x}, \quad (1)$$

where $\eta = \partial u / \partial z - \partial w / \partial x$ and b is the buoyancy with respect to some reference density $\bar{\rho}$. Consider the updraft in [Fig. 1a](#), which is strictly vertical, symmetric, and positively buoyant. From [Eq. \(1\)](#), it follows that this updraft generates positive (negative) vorticity to the right (left) of the location of maximum vertical motion w . [RKW88](#) argue that if the ascending air is lifted by a cold pool, the generation of vorticity at the outflow's edge will break the symmetry of the vorticity field, causing the updraft to tilt over the cold pool, which is illustrated in [Fig. 1b](#). The low-tropospheric shear can reduce the imbalance in the vorticity field produced by the cold pool, leading to more vertical and deeper updrafts, as shown in [Fig. 1c](#).

An "optimal" cold pool-shear relation is proposed by [RKW88](#), which constitutes the basis for quantitative diagnostics used herein, thus justifying a brief discussion on its derivation.¹ Consider the rectangular area $L < x < R$ and $0 < z < H$ in [Fig. 2](#), which includes a surface-based density current similar to the outflow of an SL. The boundaries at $x = R$, $x = L$, and $z = H$ are open, while the boundary at $z = 0$ is rigid and frictionless. The frame of reference is such that the density current's edge remains static and it is required that H be greater than the density current's depth h . Integrating the Eulerian form of [Eq. \(1\)](#) over the area in [Fig. 2](#), together with the assumptions of steadiness, with convection occurring primarily near the density current's edge (i.e., $w \approx 0$ at both $x = L$ and $x = R$), vanishing environmental buoyancy (i.e., $b = 0$ at $x = R$, where the flow at R is referred to as the environment), and static air within the outflow, obtains

$$0 = \frac{u_{H,L}^2}{2} - \frac{u_{H,R}^2}{2} + \frac{u_{0,R}^2}{2} - \int_L^R (w\eta)_H dx + \int_0^h b_L dz, \quad (2)$$

where subscripts restrict the evaluation to the respective boundary. Following [RKW88](#), we contemplate simple environmental winds u_R , with constant and positive shear below a height $z_{\text{shear}} \approx h$ and constant wind speed aloft, as shown in [Fig. 2](#). Finally, we make the following crucial assumptions: static flow at $x = L$, implying $u_{H,L} = 0$; static environmental winds above z_{shear} , implying $u_{H,R} = 0$; and a strictly vertical (i.e., optimal)

¹ For additional details, see [Bryan and Rotunno \(2014\)](#).

updraft at $z = H$, implying $\eta_H = -\partial w / \partial x$. With these assumptions, we zero out the first, second, and fourth terms in Eq. (2), leading to RKW88's optimal cold pool–shear balance condition

$$|u_{0,R}| = \left(2 \int_0^h -b_L dz \right)^{1/2} = c, \quad (3)$$

where c measures the intensity of the cold pool and $|u_{0,R}| = |u_{H,R} - u_{0,R}| = \Delta U$ measures the strength of the shear. RKW88 interpret Eq. (3) as a condition of vorticity balance between the environmental shear and the cold pool intensity required for optimal lifting of near-surface parcels. Additionally, RKW88 suggest that upshear-leaning updrafts develop in cases where the cold pool–induced circulation is dominant, characterized by $\Delta U < c$, while shear-dominated flows, characterized by $\Delta U > c$, develop downshear-leaning updrafts, which the authors refer to when explaining the life cycle of SLs. The degree of optimality is frequently diagnosed with the value of $c/\Delta U$ (e.g., Rotunno et al. 1990; WR04; BKP06; Morrison et al. 2012), with values closer to 1 corresponding to more intense and deeper updrafts.

It is important to mention that cold pool–shear balance is but one component of the total vorticity balance in an SL's updraft, which, because of its focus on cold pool–shear interactions, conceptually deemphasizes environmental upper-tropospheric shear (Fovell and Dailey 1995; WR04; Parker and Johnson 2004; Coniglio et al. 2006), latent heating of ascending air (Fovell and Tan 1998), midtropospheric buoyancy perturbations (Nicholls et al. 1988), and mesoscale circulations (e.g., Lafore and Moncrieff 1989; Weisman 1992). It is worth noting that Weisman (1992) extended RKW theory to include vorticity sources associated with rear-inflow jets, the latter being mesoscale circulations resulting mainly from within-storm latent heating (e.g., Pandya and Durran 1996). Although we acknowledge the importance that rear-inflow jets can have in the structure of SLs, herein we proceed as in WR04 by evaluating RKW theory through $c/\Delta U$, which is consistent with this investigation's focus on the deep convective line, and justified by WR04's affirmation that SL morphology can be largely explained by simple cold pool–shear relations derived from Eq. (3).

b. Layer-lifting convection: The effects of shear on latent heating under the LLMC

It is well known that many SLs have deep layers of storm-relative inflow, extending from the surface to well above the boundary layer (Kingsmill and Houze 1999;

Evans and Doswell 2001; Gale et al. 2002; Coniglio et al. 2004; Cohen et al. 2007). Such inflow can result from the propagation of a cold pool with respect to low-level winds, requiring that deep layers of air be lifted through the highly turbulent deep convective line, a process we refer to as layer-lifting convection (e.g., Bryan and Fritsch 2000; Mechem et al. 2002; AK). This form of convection differs markedly from the thermal-like conceptualization implicit in parcel theory, a distinction considered by AK to be crucial for characterizing convective instability and for interpreting the effect of shear. The LLMC conceptually embodies the layer-lifting process resulting from a propagating cold pool, wherein SL characteristics are diagnosed through system-relative fluxes of relevant parameters, computed via the propagation speed (PS) and the kinematic and thermodynamic characteristics of the environment. Figure 3 schematically illustrates the LLMC.

Regarding the effects of shear in layer-lifting storms, it is well known that latent heating produced in SLs increases as the environmental low-tropospheric shear strengthens (Fovell and Ogura 1989; Weisman 1992; AK). In accordance with the layer-lifting nature of convection in SLs, AK suggest that this dependence results largely from the environmental kinematics' modulation of inflowing convectively unstable air as a fraction of the total storm-relative inflow. The physical mechanism behind their reasoning is best explained by considering the deep convective process initiated by an SL's rapidly propagating cold pool (see Fig. 3): deep layers of low- and midtropospheric air are lifted at the cold pool's edge, leading to highly turbulent overturning motions, which initially develop as a result of potential instability triggering—for example, in moist absolutely unstable layers (Bryan and Fritsch 2000); as buoyant air ascends over the cold pool, it mixes aloft with inflowing low-equivalent potential temperature (θ_e) midlevel air, eroding the buoyancy of deep convective updrafts to an extent that depends on the relative amounts of inflowing convectively unstable air and low- θ_e midlevel air. We highlight that this process is not incorporated conceptually into RKW theory, as the latter pertains to the effects of vorticity balance for a given dilution-corrected buoyancy under parcel ascent (see discussion on the optimal state in RKW88, p. 481).

To illustrate how the low-tropospheric shear can systematically affect SLs through the aforementioned mechanism, we return to the incompressible, adiabatic, and inviscid density current in Fig. 2. As a first application of the LLMC, we are interested in environmental flow variations with changing ΔU relative to the density current's edge—that is, flow variations at R in the frame of reference where the density current's edge is static.

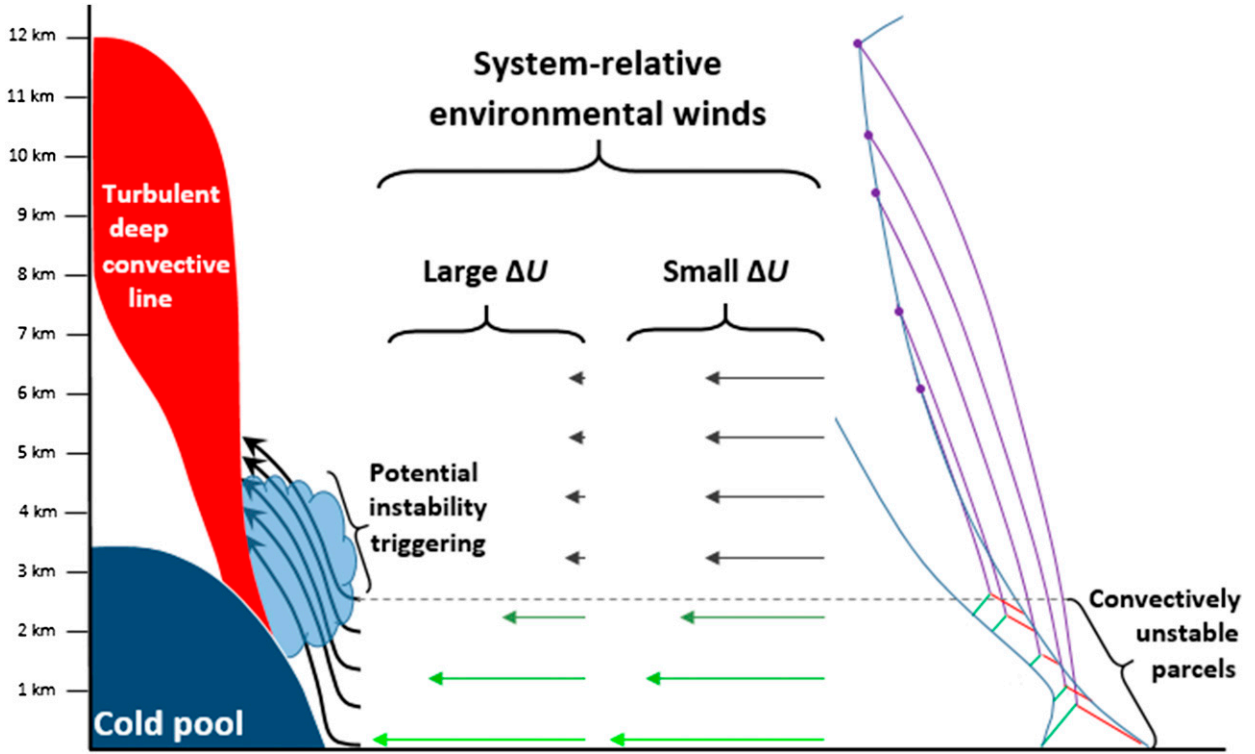


FIG. 3. Schematic representation of the LLMC, wherein the cold pool of an SL lifts deep layers of air that mix turbulently throughout the deep convective line. (right) The thermodynamic environment is depicted in a skew T - $\ln p$ chart, displaying pseudoadiabatic ascent by parcels originating at different levels. (middle) Two different cases of system-relative environmental winds with low-tropospheric shear are shown, with the color of the arrows representing the value of some relevant parameter (e.g., CAPE or the water vapor mixing ratio). The strongly sheared environment corresponds to greater inflow of convectively unstable air as a fraction of the total storm-relative inflow. See text for a more detailed explanation.

Latent heating is not incorporated into the model.² But given this study's focus on environments with low-tropospheric shear, it is reasonable to associate the air within the sheared layer (i.e., below z_{shear}) with the convectively unstable air in the context of an SL. Also, having in mind the application of the foregoing ideas to simulated SLs, we associate the open boundary at H with the tropopause (i.e., $z_{\text{tr}} = H$), although the flow is neutrally stratified. It follows that the amount of inflowing convectively unstable air as a fraction of the total tropospheric inflow is given by the shear-layer inflow fraction (SLIF), defined as

$$\text{SLIF} = \left[\int_0^{z_{\text{shear}}} \rho |u_{\text{env}} - \text{PS}| dz \right] \times \left[\int_0^{z_{\text{tr}}} \rho |u_{\text{env}} - \text{PS}| dz \right]^{-1}, \quad (4)$$

²Liu and Moncrieff (1996) analyze a steady density current model with latent heating.

where $u_{\text{env}} = u_R$ is the environmental wind profile and PS is the propagation speed of the density current's edge (PS = 0 in a frame of reference with a fixed density current's edge). Herein the SLIF is interpreted as a measure of the dilution of buoyancy resulting from kinematics under layer-lifting ascent, with larger SLIF corresponding to less dilution. We highlight that the essence of the LLMC is to contemplate environmental fluxes of inflowing air via u_{env} and the PS, as in Eq. (4).

Now we seek a functional relationship of the SLIF on ΔU . We focus on cases with $\Delta U < c$, which correspond to the majority of observed midlatitude SLs at maturity (e.g., Gale et al. 2002). For simplicity, assume an infinitely deep and steady flow, the dense fluid being static and with hydrostatic balance holding at L and R , which obtains the von Kármán formula (von Kármán 1940)

$$|u_{\text{env}}(0)| = c. \quad (5)$$

We consider environmental wind profiles of the form $u_{\text{env}}(z) = u_{\text{env}}(0) + \Delta U \times \min\{z/z_{\text{shear}}, 1\}$ with $u_{\text{env}}(0) < 0$ and $\Delta U < c$, which together with Eq. (5) imply that

$u_{\text{env}} < 0$. Under the present assumptions, the dependence of the SLIF on ΔU for given values of c and z_{shear} is given by

$$\text{SLIF} = \frac{z_{\text{shear}}(c - 0.5\Delta U)}{z_{\text{shear}}(c - 0.5\Delta U) + (c - \Delta U)(z_{\text{tr}} - z_{\text{shear}})}. \quad (6)$$

From Eq. (6), it clearly follows that, for $\Delta U < c$, the SLIF is a strictly increasing function of ΔU , such that $\text{SLIF} \rightarrow 1$ as $\Delta U \rightarrow c$; that is, the SLIF increases as the flow becomes more optimal in the sense of cold pool–shear balance. This behavior is illustrated by the two environmental wind profiles in Fig. 3, which have identical wind speeds at the surface, differing only in the strength of the shear. The more strongly sheared environment leads to greater inflow of convectively unstable air as a fraction of total storm-relative inflow over the entire troposphere, thus producing more latent heating within the deep convective region. Even though the preceding analysis contemplates a very simple flow in relation to SLs, we believe that Eq. (6) essentially captures the dependence of the SLIF on ΔU reported in Fovell and Ogura (1989) and AK. It is also worth noting that such behavior could partly account for the weakening of simulated SLs having $\Delta U < c$ with increasing $c - \Delta U$, as documented in RKW88, Weisman et al. (1988), WR04, and BKP06, among others.

c. Layer-lifting indices on the basis of convective instability under the LLMC

Considering that both low- and midtropospheric parcels ascend as a result of mechanical lifting at the cold pool's edge in the type of SLs studied herein (e.g., see AK's Fig. 11), LLMC measures of convective instability must contemplate the potential for buoyant ascent of air parcels throughout the entire atmospheric column. We do so by considering the vertical profile of CAPE—that is, CAPE computed for all tropospheric parcels. A relevant index is the vertically integrated CAPE (ICAPE), which measures the latent heating per unit area accomplished collectively by all unstable parcels as they ascend from their level of free convection (LFC) to their equilibrium level. Formally, ICAPE is defined as

$$\text{ICAPE} = \int \rho(z) \text{CAPE}(z) dz, \quad (7)$$

where $\text{CAPE}(z)$ is such that its value corresponds to the CAPE of the parcel originating at z , while the integral is taken over all levels for which $\text{CAPE}(z)$ is defined [herein CAPE refers to $\text{CAPE}(z)$]. An important characteristic of ICAPE not shared by indices computed from a parcel with properties averaged throughout a

shallow surface-based layer (e.g., MLCAPe) is that, as a consequence of the mean value theorem, ICAPE scales with the depth of the layer where CAPE is positive, rendering it as a bulk measure of convective instability in the atmospheric column (see AK).

Next, an LLMC index to measure convective instability is defined, incorporating the effects of environmental kinematics discussed in the previous subsection. We propose the mean convective instability of the storm-relative inflowing tropospheric air, which is referred to as layer-lifting CAPE (CAPE_{ll}):

$$\text{CAPE}_{\text{ll}} = \left(\int_0^{z_{\text{tr}}} \rho |u_{\text{env}} - \text{PS}| \text{CAPE} dz \right) \times \left(\int_0^{z_{\text{tr}}} \rho |u_{\text{env}} - \text{PS}| dz \right)^{-1}, \quad (8)$$

where it is assumed that $\text{CAPE} = 0 \text{ J kg}^{-1}$ for convectively stable parcels. Note that the averaging in Eq. (8) is performed over the entire troposphere, which is much deeper than the layer with $0 < \text{CAPE}$, implying that CAPE_{ll} scales with the depth of the convectively unstable layer, as does ICAPE. To separate the effects of shear from environmental thermodynamics in Eq. (8), we use Eqs. (4) and (7) to make the following approximation:

$$\text{CAPE}_{\text{ll}} \approx \left(\int_0^{z_{\text{cul}}} \rho dz \right)^{-1} \times \text{ICAPE} \times \text{SLIF}, \quad (9)$$

where z_{cul} denotes the depth of the convectively unstable layer. Equation (9) is exact in cases with $z_{\text{cul}} = z_{\text{shear}}$ and $\text{CAPE} = \text{constant}$. Given that storm-relative winds and CAPE tend to be largest near the surface, Eq. (9) underestimates CAPE_{ll} in most cases. Nonetheless, herein we consider CAPE_{ll} as defined in Eq. (9) because it clearly separates the kinematic (SLIF) and environmental thermodynamic (ICAPE) features considered relevant under the LLMC, facilitating the attribution of distinct effects that impact the convective instability available to SLs. Note that Eq. (9) incorporates the SLIF as a factor accounting for the dilution of environmental convective instability.

Below we derive several layer-lifting diagnostics from Eq. (9), which are used in later sections to validate the LLMC. For example, an index for the updraft strength w_{ll} is naturally defined as follows:

$$w_{\text{ll}} = \sqrt{2\text{CAPE}_{\text{ll}}}. \quad (10)$$

Next we define an index for the updraft slope, which is used to assess the extent to which the LLMC can account for the tilt of deep convective updrafts. This is

relevant because many studies (e.g., RKW88; Weisman 1992; Parker 2010) associate the updraft's slope with the intensity of SLs. To define an LLMC updraft slope index, we consider how system-relative environmental winds might affect the horizontal velocity of parcels ascending within the deep convective region. Following arguments by Shapiro (1992) pertaining to density current flows in deep shear environments, advective tendencies resulting from the interaction of horizontal winds with updrafts near the density current's edge are such that, the weaker the system-relative environmental wind speeds are, the more time it takes for ascending parcels to tilt in the environmental wind direction. For example, considering the two wind profiles displayed in Fig. 3, we expect the weakly sheared case, which has stronger system-relative wind speeds aloft, to have a greater impact tilting parcels in the upshear direction. This behavior can be explained in quasi-steady systems through the flow–force balance constraint, the latter having significant impacts on updraft verticality, even if $c/\Delta U$ is held fixed (Bryan and Rotunno 2014). Therefore, we define the updraft slope index m_{\parallel} by simply assuming that the horizontal velocity of deep convective updrafts is equal to the velocity of system-relative environmental winds above the shear layer ($\Delta U - \text{PS}$)³

$$m_{\parallel} = \frac{w_{\parallel}}{\Delta U - \text{PS}}. \quad (11)$$

Finally, we are also interested in defining a diagnostic for the precipitation rate (PR), which we denote as PR_{\parallel} . Taking into account that AK found the PR to be strongly dependent on the water vapor inflow rate, and considering the relevance of the strength of convection, as measured by w_{\parallel} , for the condensation rate, we define PR_{\parallel} (kg s^{-1}) as

$$\text{PR}_{\parallel} = \left(\frac{w_{\parallel}}{W}\right)^2 \times L_y \times \left[\int \rho q_v |u_{\text{env}} - \text{PS}| dz \right], \quad (12)$$

where the integral is over the troposphere, W is a constant (m s^{-1}), L_y is the length of the SL in the along-line direction, q_v is the water vapor mixing ratio, and the term in the square brackets is the water vapor inflow rate per unit length in the along-line direction ($\text{kg s}^{-1} \text{m}^{-1}$). The constant W should be selected such that $(w_{\parallel}/W)^2$

accounts for the strength of convection as well as the fact that only a small fraction of the PW falls as precipitation. Although PR_{\parallel} as defined in Eq. (12) is in kilograms per second, for readability its values are reported in units of millimeters per day.

3. Methodology

a. Numerical model

Several numerical simulations of idealized SLs were performed in three dimensions with the Cloud Model, version 1 (CM1; Bryan and Fritsch 2002). The integration of the fluid equations is done as a compressible cloud resolving model using the Klemp–Wilhelmson time-split scheme. The simulation time is 6 h. Horizontal boundaries are open in the across-line direction x and periodic in the along-line direction y . The domain extends $600 \times 100 \text{ km}^2$ (x and y directions, respectively), having a square grid spacing of 500 m. In the vertical the domain is 24 km deep, having 64 levels with grid spacing varying from 100 m near the surface to 500 m above 12 km. Several studies have shown that a grid spacing finer than the one used here is necessary to resolve relevant turbulent and microphysical processes (Bryan et al. 2003; Bryan and Morrison 2012; Lebo and Morrison 2015). Nonetheless, referring to results by Bryan et al. (2003) showing that SLs simulated with a 500-m horizontal grid spacing display the main features of storms simulated with higher resolution, we consider that the grid spacing used herein suffices for the intercase comparisons on which this study focuses.

Subgrid-scale (SGS) turbulence is accounted for by a 1.5-order closure similar to the model of Deardorff (1980). A version of the double-moment microphysics parameterization of Morrison et al. (2005) is employed for cloud (water and ice) and precipitating (rain, snow, and hail) processes. Raleigh damping is applied above 16 km with an e -folding frequency of $(300)^{-1} \text{ s}^{-1}$. The lower boundary is flat, rigid, and free slip. Surface fluxes, the Coriolis force, and radiative heat fluxes are neglected.

The initial conditions are horizontally homogeneous, as detailed in the next subsection. In order for convection to develop, we apply the horizontal wind convergence method of Morrison et al. (2015) during the first hour of simulation, determined by

$$\frac{\partial u}{\partial t} = \gamma \cos \left[\frac{\pi(x - x_c)}{2x_r} \right] \times \left[\cosh \left(\frac{2.5z}{z_r} \right) \right]^{-2},$$

where x_c is at the center of the domain, $x_r = 10 \text{ km}$ is the horizontal radius, $z_r = 10 \text{ km}$ is the maximum height where the convergence is applied and γ is a time-dependent

³ Note that the optimal cold pool–shear balance condition in Eq. (3) was derived under the assumption of vanishing system-relative environmental winds aloft, thus acknowledging the importance of for determining updraft verticality. Furthermore, in density current simulations supporting RKW theory (e.g., RKW88; WR04; Bryan and Rotunno 2014), updrafts tend to tilt in the direction determined by $\text{PS} - \Delta U$, with optimal flows achieved when $\text{PS} \approx \Delta U$.

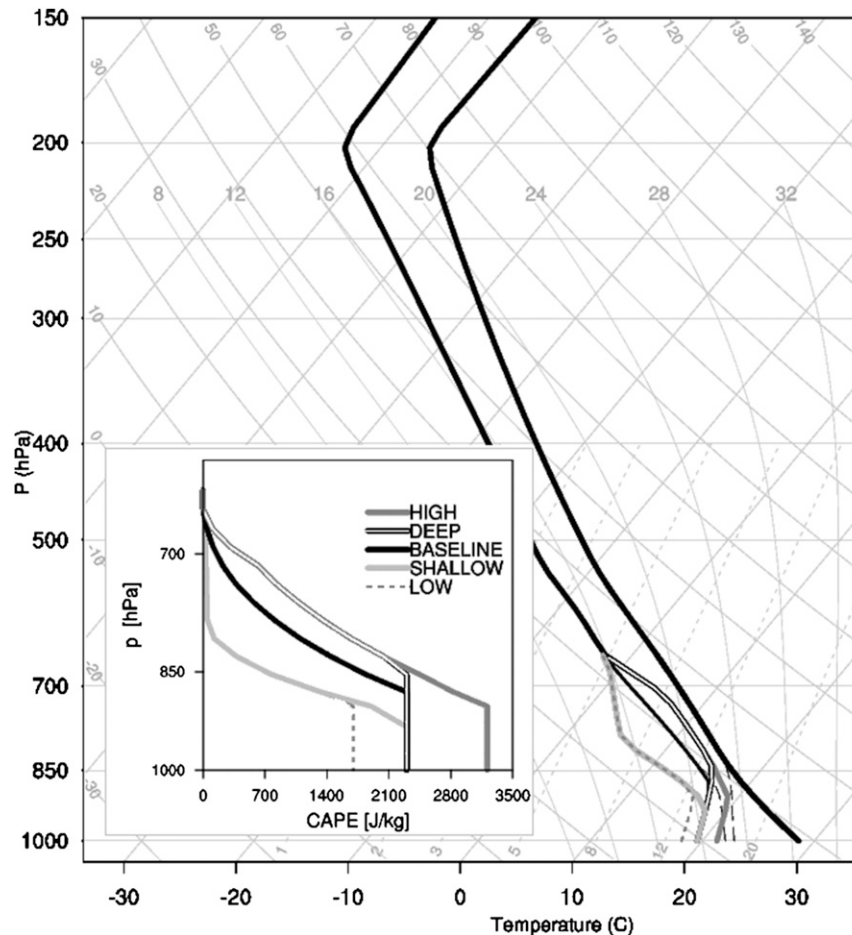


FIG. 4. Skew T - $\ln p$ chart showing the thermodynamic environments under consideration, with their respective $\text{CAPE}(p)$ shown in the inset. The soundings are identified by the line pattern and color of the dewpoint temperature curve according to the labels in the plot of $\text{CAPE}(p)$. All environments have identical temperatures and dewpoint temperatures above 850 and 650 hPa, respectively. The sounding represented by the thin black dashed lines corresponds to STABLE, which is the only case with temperatures that differ from those of BASELINE.

variable equal to 0.1 m s^{-2} between initiation and 3000 s, linearly decreasing to 0 m s^{-2} at 3600 s. Random temperature perturbations of up to 0.1-K amplitude are added at initialization, in the region of convergence forcing, in order for the system to develop three dimensionality.

b. Environmental thermodynamics and kinematics

Several thermodynamic environments are specified with the method described in AK via vertical profiles of CAPE and LFC. The environments are meant to resemble severe weather conditions in the continental United States (e.g., Bluestein and Jain 1985). For simplicity in the interpretation of results, focus is placed on one temperature profile, determined in the lower and

middle troposphere by CAPE as a function of pseudoentropy (see the appendix in AK), while at upper levels we use the analytical sounding of Weisman and Klemp (1982). With the exception of a sounding with relatively high dry static stability near the surface, the soundings under consideration differ exclusively in their moisture at low and middle levels. The soundings and their corresponding CAPE profiles are shown in Fig. 4.

Some relevant characteristics of the thermodynamic environments are displayed in Table 1. In ascending order of ICAPE and precipitable water (PW), the environments are referred to as LOW [with the lowest most unstable CAPE (MUCAPE)], SHALLOW (with the shallowest MUCAPE layer), BASELINE (similar to the sounding used in RKW88), STABLE (same

TABLE 1. Diagnostics of the thermodynamic environments.

	MUCAPE (J kg^{-1})	ICAPE ($\text{J m}^{-2} \times 10^{-6}$)	PW (kg m^{-2})
LOW	1700	2.6	39.4
SHALLOW	2300	3.2	40.4
BASELINE	2300	4.7	44.7
STABLE	2300	4.7	46.6
DEEP	2300	5.6	46.9
HIGH	3300	6.8	49

CAPE profile as BASELINE, but strongly stratified and relatively moist near the surface), DEEP (with the deepest MUCAPE layer), and HIGH (with the highest MUCAPE). Referring to the CAPE profiles in Fig. 4, we highlight that SHALLOW, BASELINE, STABLE, and DEEP have the same CAPE below 920 hPa, with DEEP and HIGH having identical CAPE and moisture profiles above 850 hPa, and similarly for SHALLOW and LOW above 880 hPa. We include STABLE, which resembles nocturnal conditions, for two reasons: first because AK found that high dry static stability at low levels has relevant impacts for the PS of SLs, thus affecting CAPE_{II} for a given ICAPE and ΔU [see Eqs. (4) and (9)]; second, because the cold pool intensity might be modified for a given ICAPE through low-tropospheric temperature variations.

The kinematic environments under consideration have static winds in the along-line direction, while winds in the across-line direction have constant shear below 3.5 km and constant wind speeds aloft. The depth of the shear layer is chosen to overlap with the convectively unstable layer of the soundings in Fig. 4, justifying the approximation in Eq. (9). This study contemplates the five wind profiles shown in Fig. 5, having $\Delta U = 5, 10, 16, 22$, and 28 m s^{-1} over the lowermost 3.5 km, which spans much of the range of low-tropospheric shear found in observations (e.g., Evans and Doswell 2001). The domain is translated at a constant across-line speed of 17, 17, 20, 25, and 28 m s^{-1} for the $\Delta U = 5, 10, 16, 22$, and 28 m s^{-1} environments, respectively, in order for the storms to remain distanced from the lateral boundaries. Results presented below are derived from simulations performed under every combination of thermodynamic and kinematic environments described in this subsection, and the simulations will be identified by their thermodynamic environment underscore ΔU (e.g., LOW_16).

4. Results

a. Basic diagnostics of the simulated SLs

Some basic diagnostics of the simulated SLs are shown in Table 2. Their values were computed by averaging the

respective variable between 3.75 and 4.25 h, a period that we take as representative of the mature stage. In addition, Table 3 shows layer-lifting and cold pool–shear balance diagnostics deduced from the PS and $\bar{\tau}$ reported in Table 2. Further details about the definition of these variables are given below.

First we discuss the cold pool intensity,

$$c = \left[\frac{2}{\bar{\rho}(0)} \int_0^h \bar{\rho} b \, dz \right]^{1/2},$$

where $\bar{\rho}$ is the initial/environmental density profile, with respect to which the buoyancy b is defined, and h is the depth of the cold pool—that is, the contiguous surface-based layer where $b < 0$. Given that c varies throughout the entire horizontal domain, we consider an averaged value \bar{c} given by

$$\bar{c} = \frac{1}{L_{\bar{\tau}}} \int_{x_{\bar{\tau}} - 0.5L_{\bar{\tau}}}^{x_{\bar{\tau}} + 0.5L_{\bar{\tau}}} \left(\frac{1}{L_y} \int_0^{L_y} c \, dy \right) dx, \quad (13)$$

where L_y is the along-line extent of the domain (herein 100 km), $x_{\bar{\tau}}$ is the across-line location where the term in

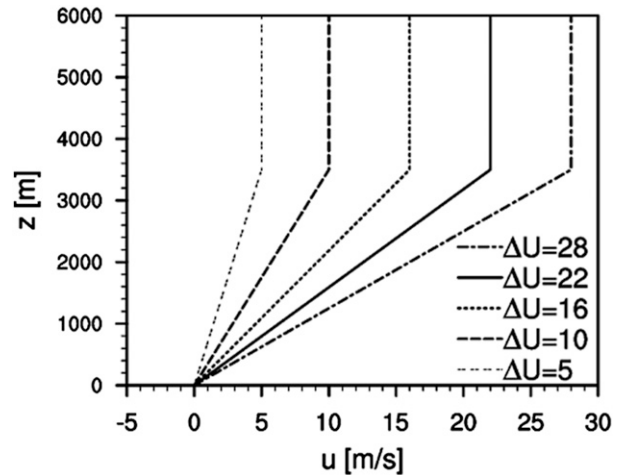


FIG. 5. Profiles of horizontal winds (across-line direction) used in association to each sounding in Fig. 3. In all cases the wind velocity is constant above 3.5 km.

TABLE 2. Diagnostics of all simulations, with values averaged between 3.75 and 4.25 h of simulation time. PS, w_{\max} , \bar{c} , and \bar{B} are in units of m s^{-1} , PR is in units of mm day^{-1} , and SLIF is a fraction (see text for more details).

	LOW					SHALLOW					BASELINE				
ΔU	5	10	16	22	28	5	10	16	22	28	5	10	16	22	28
PS	16	18	23	24	26	17	20	23	25	26	19	20	23	26	28
w_{\max}	21	22	29	32	40	25	28	32	36	43	30	32	37	44	50
PR	5	11	24	30	35	12	19	31	37	38	31	39	46	51	55
\bar{c}	17	18	29	30	32	23	27	30	32	33	29	28	33	37	40
\bar{B}	15	21	24	25	31	21	25	26	27	32	27	28	30	32	35
SLIF	0.49	0.55	0.62	0.81	0.81	0.48	0.54	0.63	0.80	0.81	0.48	0.53	0.63	0.74	0.99

	STABLE					DEEP					HIGH				
ΔU	5	10	16	22	28	5	10	16	22	28	5	10	16	22	28
PS	16	17	21	25	26	19	21	23	27	29	19	21	23	27	29
w_{\max}	29	31	38	44	49	30	33	39	45	51	36	38	42	48	53
PR	30	34	45	51	58	37	46	54	59	62	48	55	63	67	68
\bar{c}	30	30	33	38	38	29	33	35	39	40	32	33	36	40	42
\bar{B}	28	29	31	33	35	29	31	32	35	38	33	33	35	37	40
SLIF	0.49	0.57	0.66	0.80	0.86	0.48	0.53	0.63	0.71	0.92	0.48	0.53	0.62	0.71	0.93

parentheses (the along-line average of c) attains its maximum value, while $L_{\bar{c}}$ is the length of the interval for averaging around $x_{\bar{c}}$ (herein 10 km). Figure 6 illustrates the across-line region over which c is averaged in Eq. (13).

It is worth highlighting that the range of \bar{c} simulated herein, spanning values between 17.3 m s^{-1} (LOW_5) and 42.2 m s^{-1} (HIGH_22), overlaps considerably with observationally derived values reported in Bryan et al. (2005). These cold pool intensities encompass greater intercase variability than contemplated in previous studies (e.g., WR04; BKP06), which we attribute to differences in the thermodynamic environment. This is illustrated by the scatterplot in Fig. 7a displaying all simulations in terms of their ICAPE (abscissa) and their \bar{c} (ordinate), corroborating AK's finding that

higher ICAPE favors the development of larger \bar{c} , for a given ΔU .

Figure 7a also reveals that, for a given ICAPE, greater ΔU leads to larger \bar{c} , which is a well-known behavior of simulated SLs with $\Delta U < \bar{c}$ (e.g., BKP06). Interestingly, by comparing scatterplots in Figs. 7a and Fig. 7b, the latter showing tighter clustering of points around a curve with \bar{c} as a monotonically increasing function of CAPE_{II} , it appears that the dependence of \bar{c} on ΔU is partly accounted for by latent heating via the SLIF [see Eq. (9)]. Indeed, Fig. 8, which displays all storms in terms of their PS – ΔU (abscissa) and their SLIF (ordinate; see Table 2), clearly shows that, for a given thermodynamic environment, stronger shear favors higher SLIF, and thus a larger fraction of inflowing convectively unstable air compared to the inflow of midtropospheric air with low

TABLE 3. The values of cold pool–shear balance ($\bar{c}/\Delta U$) and layer-lifting indices (w_{II} , PR_{II} , and $1/m_{\text{II}}$) derived from \bar{c} and PS in Table 2. The indices w_{II} and PR_{II} have units of m s^{-1} and mm day^{-1} , respectively, and m_{II} is dimensionless (we report $1/m_{\text{II}}$ because very large values of m_{II} arise for high ΔU). The value of W used to calculate PR_{II} in Eq. (9) is set to 66 m s^{-1} .

	LOW					SHALLOW					BASELINE				
ΔU	5	10	16	22	28	5	10	16	22	28	5	10	16	22	28
$\bar{c}/\Delta U$	3.5	1.8	1.8	1.4	1.2	4.6	2.7	1.9	1.4	1.2	5.7	3	2.1	1.7	1.4
w_{II}	26	28	29	33	34	29	30	34	37	37	35	36	40	43	50
PR_{II}	12	13	17	20	19	16	19	21	25	24	29	31	35	42	52
$1/m_{\text{II}}$	0.42	0.31	0.25	0.07	−0.07	0.44	0.34	0.2	0.07	−0.06	0.41	0.29	0.17	0.1	0

	STABLE					DEEP					HIGH				
ΔU	5	10	16	22	28	5	10	16	22	28	5	10	16	22	28
$\bar{c}/\Delta U$	5.9	2.8	2.1	1.7	1.4	5.9	3.3	2.2	1.8	1.4	6.4	3.3	2.3	1.8	1.5
w_{II}	35	38	41	45	46	38	40	44	46	52	42	44	47	51	58
PR_{II}	25	27	35	44	44	36	39	44	53	64	45	50	57	69	83
$1/m_{\text{II}}$	0.3	0.19	0.13	0.06	−0.04	0.37	0.28	0.16	0.11	0.02	0.33	0.25	0.16	0.1	0.01

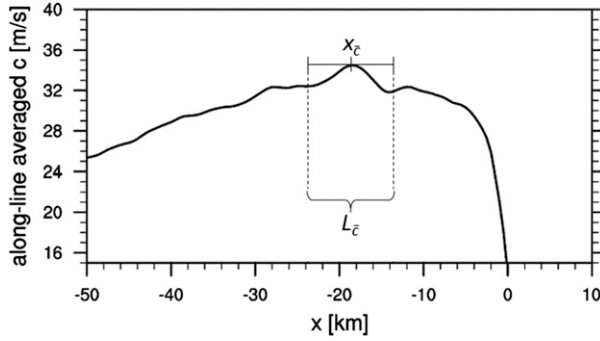


FIG. 6. Along-line-averaged c corresponding to BASELINE_16 at 4-h simulation time. The location of the maximum value is denoted by x_c , and the across-line region for averaging c in Eq. (10) is located within the dashed lines.

θ_e . The relation between cold pool development and convective instability under the LLMC probably results from the direct link between the rate of hydrometeor production and latent heating under layer-lifting ascent (see AK), the latter being closely related to CAPE_{II} in the present simulations, as shown below.

Next we evaluate the appropriateness of CAPE_{II} for characterizing convective instability in the present simulations. To this end, we measure the amplitude of latent heating produced by the SLs and determine whether an apparent relationship with CAPE_{II} exists. Latent heating is measured with the storm-induced buoyancy above the cold pool \bar{B} (see Table 2), which is defined by an average analogous to that in Eq. (13), applied to the following variable:

$$B = \left[\frac{2}{\bar{\rho}(0)} \int_h^{z_{\text{tr}}} \bar{\rho} b \, dz \right]^{1/2}.$$

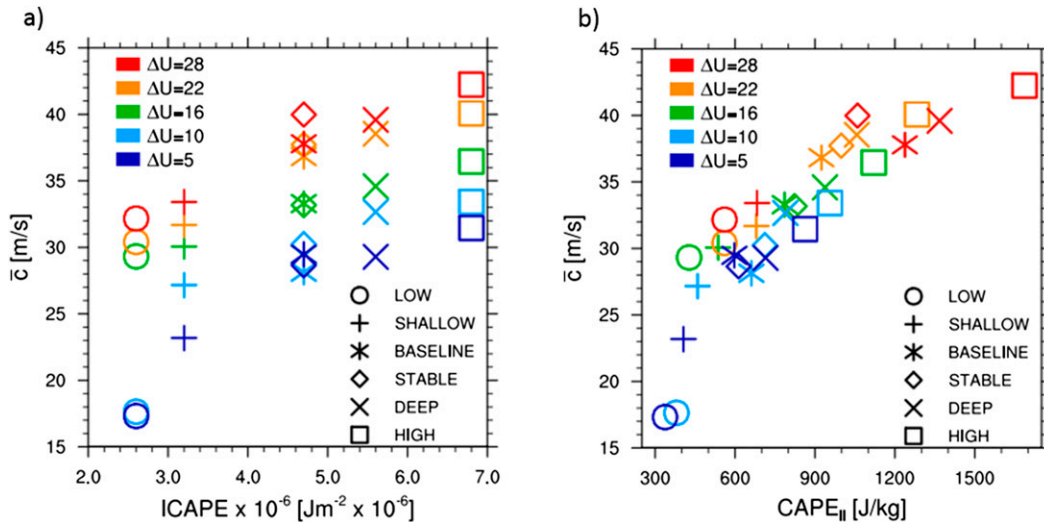


FIG. 7. Scatterplot representing all simulations (a) on an ICAPE– \bar{c} plane and (b) on a CAPE_{II} – \bar{c} plane.

Scatterplots in Fig. 9 show similar patterns to those in Fig. 7 in terms of the variability of \bar{B} , its apparent dependence on ICAPE and ΔU in Fig. 9a, as well the tight and monotonically increasing relationship between \bar{B} and CAPE_{II} in Fig. 9b. The tighter correspondence of \bar{B} with CAPE_{II} (Fig. 9b) than with ICAPE (Fig. 9a) lends weight to the relevance of shear for modulating the mean convective instability of the storm-relative inflow. We think that these results support CAPE_{II} as a suitable index for diagnosing convective instability in SLs, allowing a more general evaluation of the LLMC.

b. Layer-lifting indices as diagnostics for PR, w_{max} , and updraft verticality

In this subsection we analyze the diagnostic skill of layer-lifting indices (see subsection 2c and Table 3). As a result of the wide range of \bar{c} attained herein, the intercase variability of $\bar{c}/\Delta U$ is considerably larger than that contemplated in previous numerical investigations of mature SLs (e.g., cases with $\Delta U < \bar{c}$ in BKP06). Nonetheless, all simulated storms have $\Delta U < \bar{c}$ at maturity, as do many midlatitude SLs in the central United States, in which the LLMC is most relevant. These SLs are often characterized by $c \approx 30 \text{ m s}^{-1}$ and rarely occur in environments with $25 \text{ m s}^{-1} < \Delta U$, even when ΔU is computed over deeper layers (Evans and Doswell 2001; Gale et al. 2002; SCDE05). In agreement with RKW theory, the SLs under consideration developed upshear-leaning updrafts, as will be shown below.

Figure 10 displays the evolution of w_{max} (Figs. 10a and 10b) and PR (Figs. 10c and 10d) of all simulations. The lines in Figs. 10a and 10c are colored by w_{II} and

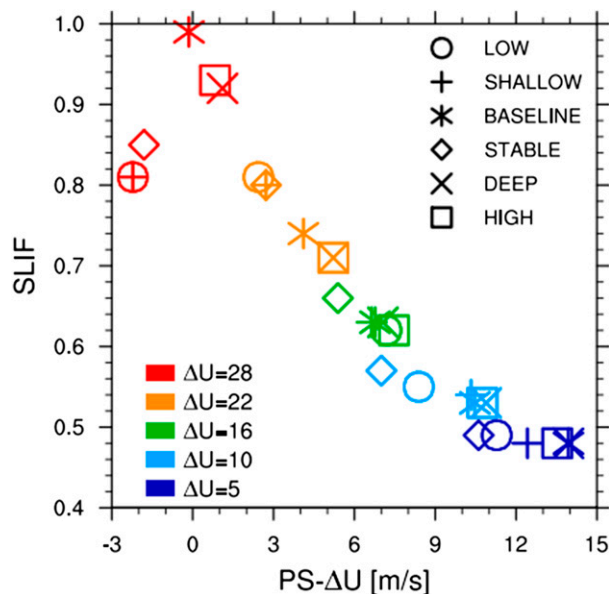


FIG. 8. As in Fig. 7, but on a $(PS - \Delta U)$ -SLIF plane.

PR_{II} , respectively, as determined by the label bars. Throughout the simulation time, the vertical distribution of the line colors is in broad agreement with the color gradient of their respective label bars, suggesting that w_{II} and PR_{II} have considerable diagnostic skill. Such skill does not result from cold pool-shear balance effects, as suggested by the relatively weak correspondence between the vertical distribution of line colors in Figs. 10b and 10d, determined by $\Delta U/\bar{c}$, and their label bars.⁴ It is also worth mentioning that ICAPE is also a poor diagnostic for both w_{max} (shown below) and PR (see Table 3).

A more quantitative attribution of distinct impacts that environmental shear has on the updraft strength can be accomplished with the aid of regression analysis. First, we perform a least squares linear regression of w_{max} on ICAPE (Fig. 11a) and of w_{max} on w_{II} (Fig. 11b). The linearity assumption is justified by visual inspection of the scatterplots in Fig. 11, with Fig. 11b showing a surprisingly tight linear relationship between w_{max} and w_{II} . The fraction of variance unexplained by ICAPE equals 0.7, a value that drops to 0.16 when w_{II} is used as the predictor variable (see r^2 values in Fig. 11). This result shows that ΔU accounts for much of the variability in updraft intensity through its effects on latent heating. It is worth highlighting that the large diagnostic skill of w_{II} leaves little room for improvement within the simulations under consideration, with similar results holding

for PR_{II} (not shown).⁵ For example, after controlling for convective instability under the LLMC by subtracting the w_{II} -regression line from w_{max} , we find that a linear regression of the residuals on $\Delta U/\bar{c}$, as shown in Fig. 11c, contributes to explain $0.64 \times 0.16 \approx 0.1$ of the total variance of w_{max} . This analysis shows that updraft strength variations are largely accounted for by convective instability as measured with the LLMC, with shear playing a major role through its impact on $CAPE_{II}$ via the SLIF.

Next, we consider trajectories corresponding to deep convective updrafts, as revealed by Lagrangian particles originating at $z = 350$ m and $x \approx 10$ km ahead of the cold pool's edge at 4 h of simulation time. Within each simulation the particles differ exclusively in their along-line location, with one particle placed every 2 km. Particle positions are calculated every time step by trilinear interpolation and we use output produced every 2.5 min. The average trajectory of deep convective particles computed for each simulation is shown in Fig. 12. We define as deep convective particles those that reach above 8 km height 45 min after they originate (i.e., at 4.75 h of simulation time), with the average trajectory determined by

$$\overline{[x(s), z(s)]} = \left\{ \sum_{i \in I} [x(s), z(s)]_i \right\} / N,$$

where $(x, z)_i$ is the i th trajectory relative to the cold pool edge, I is the set containing indices corresponding to deep convective particles, N is the number of elements in I , and s is the length of the trajectory starting at $[x(0), z(0)]_i = (8 \text{ km}, 350 \text{ m})$. The trajectories are colored according to ΔU (Fig. 12a), $\Delta U/\bar{c}$ (Fig. 12b), ICAPE (Fig. 12c), and m_{II}^{-1} (Fig. 12d). Surprisingly, $\Delta U/\bar{c}$ does not improve on the correspondence of ΔU with trajectory verticality, with the latter having a larger Pearson correlation coefficient with the $z = 350$ -m to $z = 5$ -km trajectory slope than $\Delta U/\bar{c}$ (0.76 vs 0.63). This observation is in support of SCDE05, who argue that cold pool-shear balance derives its skill mainly from variations in ΔU . Also note that ICAPE does not appear to significantly constrain trajectory verticality (Fig. 12c), while m_{II}^{-1} is the best discriminator of that feature, having a 0.83 Pearson correlation coefficient with the $z = 350$ -m to $z = 5$ -km trajectory slope. These results suggest that the updraft tilt is strongly constrained by ΔU , which modulates both the horizontal environmental wind speed aloft, thus affecting the updraft's horizontal velocity (see section 2c), and latent heating via the SLIF (see section 2b and Fig. 8), which ultimately determines the updraft's vertical velocity. The updraft slope index m_{II}

⁴ For visual clarity, cold pool-shear balanced is diagnosed with $\Delta U/\bar{c}$ in figures throughout this subsection.

⁵ The linear regression of w_{max} on w_{II} gives a slope almost identical to 1 and a relatively small intercept (-3.2), lending weight to the LLMC.

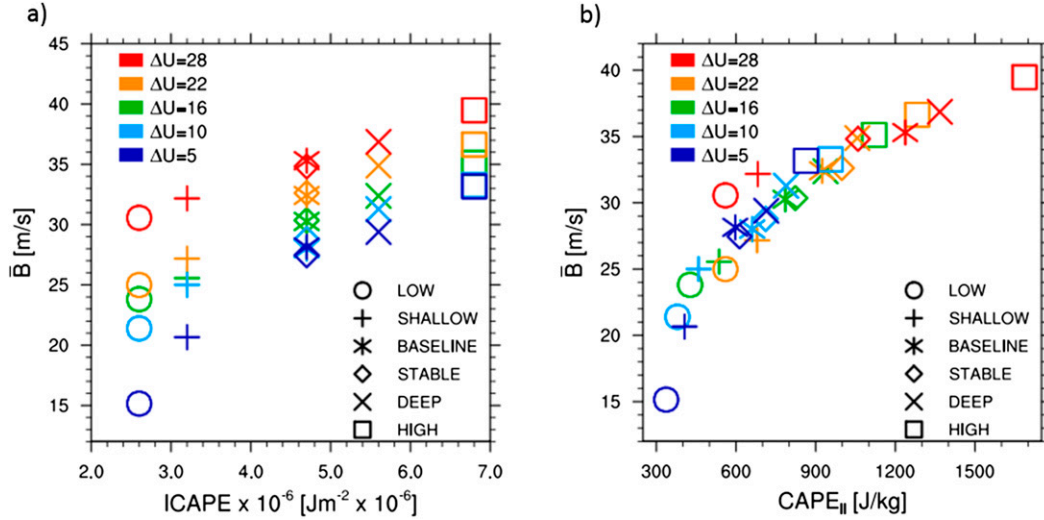


FIG. 9. As in Fig. 7, but (a) on an ICAPE– \bar{B} plane and (b) on a CAPE_{II}– \bar{B} plane.

appears to largely account for those features; however, it is important to note that the upshear tilt of deep convective updrafts is conceptually inconsistent with $m_{II} < 0$ (see $\Delta U = 28$ simulations in Table 3), as the latter corresponds to downshear-leaning updrafts.

c. Intercase comparisons of radar reflectivity, buoyancy, and horizontal winds

In this section we compare some fields of interest produced at 4 h of simulation time by selected storms.

Figure 13 shows the radar reflectivity in the horizontal plane at $z = 1$ km corresponding to LOW₁₀, SHALLOW₁₆, and HIGH₂₂, which were selected because they produce similar $\bar{c}/\Delta U$ in varying kinematic and thermodynamic environments. The contrasting appearance between the deep convective region in LOW₁₀ (Fig. 13a) and HIGH₂₂ (Fig. 13c) is notable, with the latter displaying a discontinuous cellular structure within the high-reflectivity region, while the latter appears more slabular, as described by James et al.

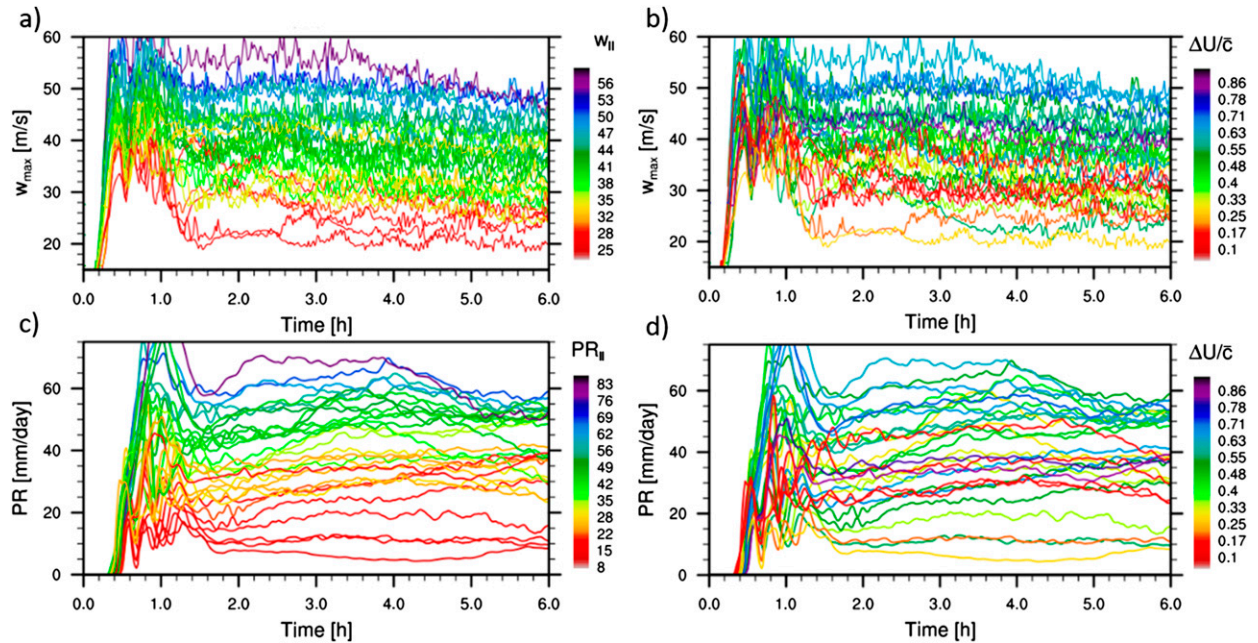


FIG. 10. The evolution of (a),(b) w_{max} and (c),(d) PR of all simulations is shown. Colors in (a) and (c) correspond to w_{II} and PR_{II} , respectively, while each curve in (b) and (d) is colored according to $\Delta U/\bar{c}$, as determined by the label bars.

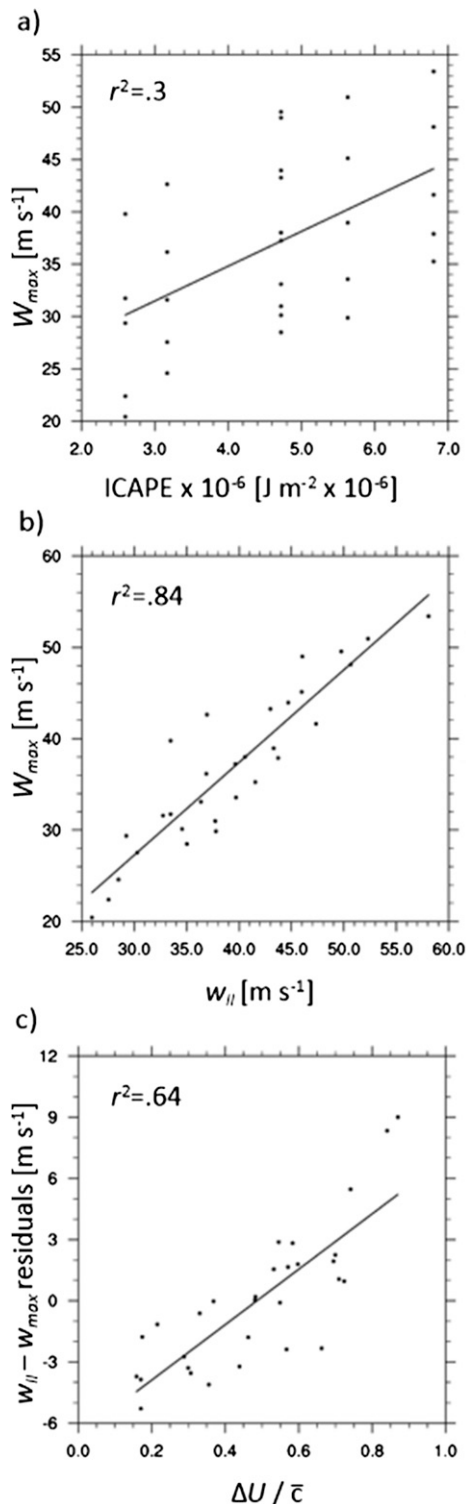


FIG. 11. Scatterplots and least squares linear regression model relating (a) ICAPE (explanatory variable) and w_{\max} (dependent variable), (b) w_{11} (explanatory variable) and w_{\max} (dependent variable), and (c) $\Delta U / \bar{\sigma}$ (explanatory variable) and [residuals from the w_{11} regression model in (b)] (dependent variable). The r^2 values are reported at the top-left corner of each panel.

(2005). Such contrasting behavior for a given value of $\bar{\sigma} / \Delta U$ is possible because, in the environments considered herein, the most intense SLs are the ones that produce the strongest cold pools; therefore, storms in high-ICAPE and strongly sheared environments, which develop large $\bar{\sigma}$, may attain similar $\bar{\sigma} / \Delta U$ to storms in low-ICAPE and weakly sheared environments, given that the latter produce small $\bar{\sigma}$. It follows that, if such relationship between ICAPE and cold pool intensity generally holds in naturally occurring SLs (see Fig. 7a), $\bar{\sigma} / \Delta U$ would be of limited operational value.

In analogy with the preceding analysis, now we consider the radar reflectivity plots in Fig. 14, corresponding to DEEP_5, BASELINE_10, and SHALLOW_22, which produced $w_{11} \approx 36 \text{ m s}^{-1}$. The reflectivity plots in Fig. 14 have a similar appearance within the deep convective region, especially in relation to the contrasting behavior portrayed in Fig. 13 and despite large differences in $\bar{\sigma} / \Delta U$. The convective mode displayed by the SLs in Fig. 14, which resembles the reflectivity structure in Fig. 13b, appears to be an intermediate case between the cellular and slabular SLs in Figs. 13a and 13c, respectively. It is worth highlighting that w_{11} is a good discriminator of the subjectively determined convective mode among all simulations considered herein (not shown), with $w_{11} < 30 \text{ m s}^{-1}$ corresponding to cellular structures, $w_{11} > 45 \text{ m s}^{-1}$ representing slabular storms, and the rest having intermediate structures.

The kinematic and buoyancy structure of selected simulations is displayed in Fig. 15, showing contour plots of along-line averaged horizontal winds and buoyancy. First, we note that the strength of the environmental shear by itself has a significant impact on the mesoscale structure of SLs. For instance, larger ΔU is associated with horizontally narrower storms and a greater difference in midtropospheric horizontal wind speeds across the leading edge of the system. Neither w_{11} or $\bar{\sigma} / \Delta U$ are suitable diagnostics for these mesoscale features. Nonetheless, w_{11} appears to have diagnostic skill for the intensity of mesoscale circulations and, in agreement with Figs. 7b and 9b, the amplitude of within-storm buoyancies. For instance, DEEP_5 and SHALLOW_22 (Figs. 15c and 15d, respectively), with $w_{11} \approx 36 \text{ m s}^{-1}$, attained similar amplitude of maximum within-storm buoyancies aloft (around 0.16 m s^{-2}) and maximum horizontal wind speeds in both the middle troposphere ($\approx 25 \text{ m s}^{-1}$) and within the cold pool ($\approx 7 \text{ m s}^{-1}$), notwithstanding large differences in ICAPE, ΔU , and $\bar{\sigma} / \Delta U$. On the other hand, the simulations in Fig. 15 that produce the smallest and largest perturbation fields are LOW_10 (Fig. 15a) and HIGH_22 (Fig. 15b), respectively, consistent with their w_{11} values and despite having similar $\bar{\sigma} / \Delta U$. These results, which are broadly

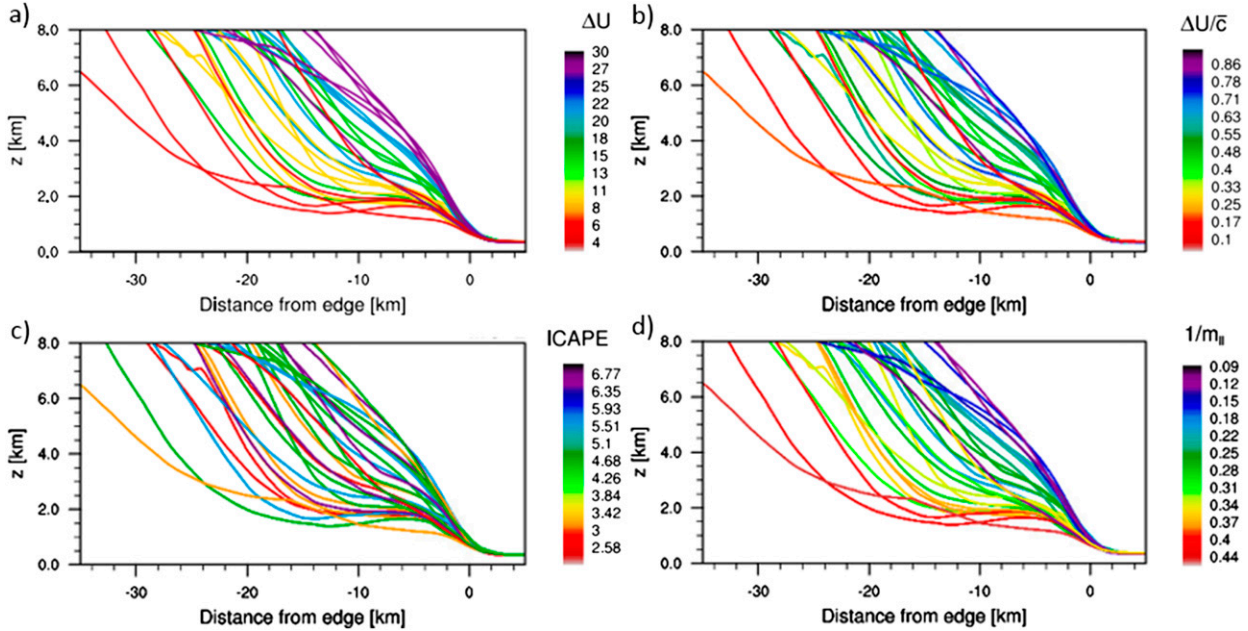


FIG. 12. Average trajectories of deep convective Lagrangian particles of all simulations (see text for more details), except LOW_5, which did not develop deep convective trajectories. Trajectories are colored according to (a) ΔU , (b) $\Delta U/\bar{c}$, (c) ICAPE, and (d) $m_{||}^{-1}$.

representative of the behavior of simulations considered herein, support the physical significance of $w_{||}$, further indicating the importance of ΔU , but failing to provide a clear picture regarding cold pool–shear balance effects.

5. Discussion

a. PS as an internal control of SL intensity in the LLMC

Having shown the diagnostic skill of layer-lifting indices, it is worth discussing the optimal shear strength for the intensity of SLs, as implied by the LLMC, for a given thermodynamic environment. In other words, we look for ΔU that maximizes $\text{CAPE}_{||}$, for a given ICAPE. Referring to Eqs. (4) and (9), it follows that $\text{CAPE}_{||}$ is maximized when $\text{SLIF} = 1$ —that is, when $\Delta U = \text{PS}$.

The ubiquitousness of the optimality condition of vanishing system-relative environmental winds aloft is worth highlighting, being proposed by Thorpe et al. (1982), and assumed to hold when deriving the cold pool–shear balance condition in Eq. (3). Additionally, density current studies of Shapiro (1992) and Moncrieff and Liu (1999), as well as the SL investigation of Coniglio et al. (2006), indicate the importance of winds aloft for producing deep ascent in environments with deep tropospheric shear. However, it is important to note that arguments presented in the aforementioned investigations, which emphasize the kinematic structure

of updrafts as directly affected by environmental winds, differ fundamentally from the modulation of latent heating by ΔU on which this study focuses. While it is undeniable that environmental shear directly affects the organization of storms in a fundamental way (e.g., Parker and Johnson 2004), results presented herein suggest that, when shear is confined to low levels, updraft structure and intensity in mature SLs is largely constrained by latent heating under layer-lifting convection.

We find strong support for the importance of the storm-relative inflow in observational studies of proximity soundings within the continental United States, with results that appear consistent with our findings regarding the relevance of the SLIF. For instance, Evans and Doswell (2001) found that weakly forced derecho events have weak mid-tropospheric inflow, implying a large SLIF and perhaps explaining the severe weather potential of such storms. In addition, Cohen et al. (2007) showed that, for storms with similar inflow at middle levels, the low-level inflow is an excellent discriminator for the strength of the surface winds produced by SLs; in other words, considering that the intensity of surface wind speeds is closely related to the PS, while the latter tends to be larger in more intense storms within cases considered herein (see Table 2), results in Cohen et al. (2007) suggest that the most intense SLs are precisely those with greatest SLIF. Furthermore, Gale et al. (2002) consistently observed a decrease in the system-relative inflow at low levels, wherein convectively unstable air resides, prior to the dissipation of nocturnal

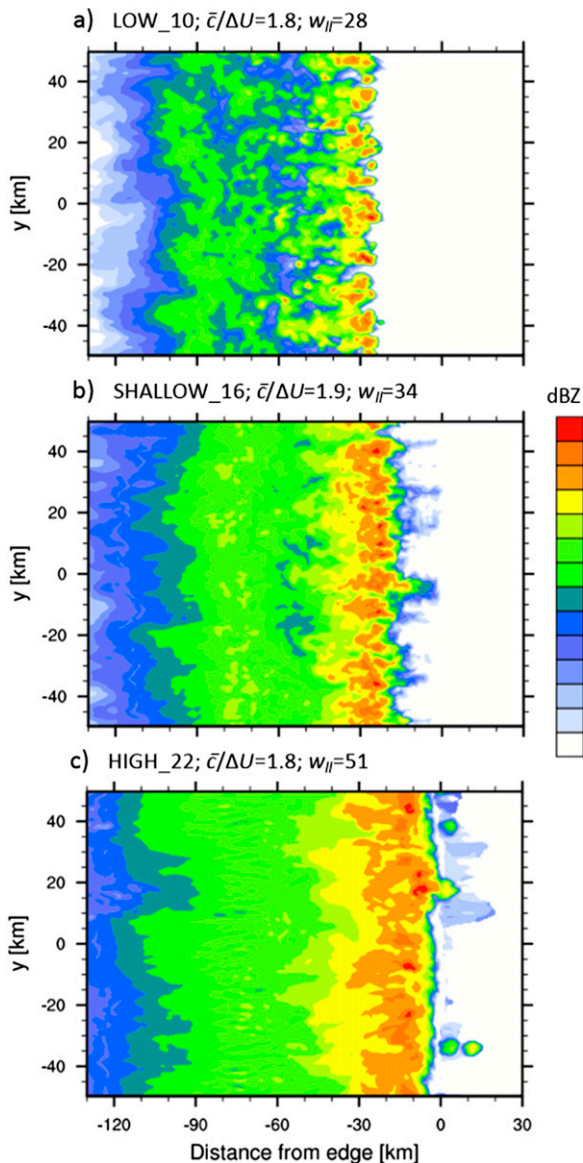


FIG. 13. Contour plots of radar reflectivity (dBZ) on the horizontal plane at 1-km height at 4-h simulation time, corresponding to (a) LOW_10, (b) SHALLOW_16, and (c) HIGH_22.

mesoscale convective systems. Observationally based analyses thus appear to be consistent with the LLMC, although a more detailed analysis is required to make a precise attribution of latent heating effects.

It is worth noting that all LLMC indices defined in section 2c depend exclusively on the PS and environmental thermodynamics and kinematics. Working with the PS is advantageous for conducting an observational validation of the LLMC, which can be estimated with surface observations and radar reflectivity images. On the other hand, the cold pool intensity requires vertical profiles of both environmental and within-storm

thermodynamics, for which data are currently sparse in both space and time, thus complicating an observational assessment of RKW theory.

b. The application of RKW theory to SLs

Results presented herein do not provide clear indication that mature SLs are strongly constrained by cold pool–shear balance. For instance, we find better correspondence between several metrics of system intensity (e.g., w_{\max} , the updraft slope and the strength of mesoscale circulations) with ΔU than with $\bar{c}/\Delta U$, which is in agreement with observations by SCDE05. As mentioned in section 4c, this state of affairs could arise because, for cold pool–dominated storms, as those analyzed herein, the most intense SLs tend to develop larger \bar{c} , while, according to RKW theory, system strength should vary inversely with \bar{c} in such cases. While such behavior does not invalidate the relevance of cold pool–shear balance circulations, it is indicative of the low-tropospheric shear primarily impacting on SL intensity through latent heating effects, with vorticity balance playing a secondary role.

It is possible that a more robust vorticity balance diagnostic than $\bar{c}/\Delta U$ could allow a clearer identification of the workings of RKW theory. But upon incorporating circulations within the cold pool into the vorticity budget, as in Weisman (1992), the performance of vorticity balance diagnostics does not improve noticeably in simulations presented herein (not shown).⁶ For instance, the difference in vorticity balance between DEEP_5 and SHALLOW_22 increases, notwithstanding similarities in the amplitude of their perturbation fields (see section 4c); additionally, when using the vorticity balance diagnostic of Weisman (1992), simulations with $\Delta U = 28$ appear as shear-dominated flows, while their updrafts lean upshear (see Fig. 12).

Regarding the implications for the applicability of RKW theory to mature SLs, it is important to address the appropriateness of assessing cold pool–shear balance by comparing the morphology of storms simulated in varying thermodynamic environments. First, we note that latent heating is not intrinsically predicted nor diagnosed by RKW theory, so an assessment of cold pool–shear balance should ideally proceed by comparing the structure of SLs with varying $c/\Delta U$, for a given amount of latent heating within the deep convective region.⁷ Having

⁶ The vorticity associated with cold pool kinematics is computed as the difference between the maximum along-line-averaged horizontal wind speed within the cold pool and the surface wind speed at the same across-line location.

⁷ Effects of latent heating/cooling are incorporated into RKW theory as exogenous parameters—namely, cold pool kinematic and thermodynamic characteristics.

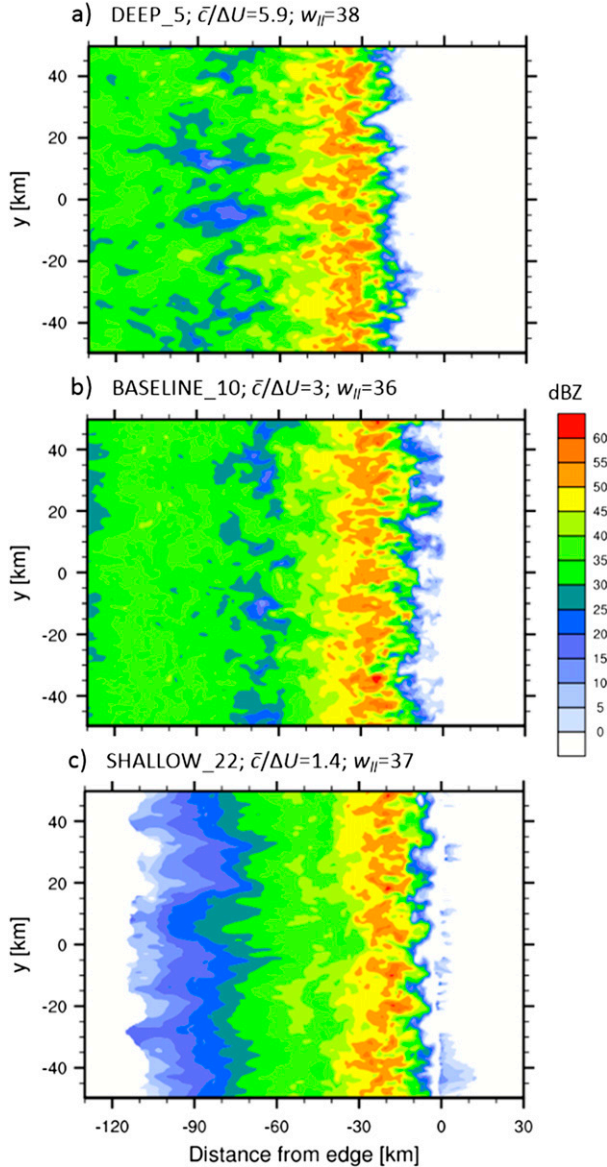


FIG. 14. As in Fig. 13, but corresponding to (a) DEEP_5, (b) BASELINE_10, and (c) SHALLOW_22.

discussed how shear can affect latent heating via the SLIF, and given that, for a fixed thermodynamic environment, the more cold pool–shear balanced SLs among the simulations under consideration also have the greatest available convective instability, as measured by CAPE_{II} , we contend that not only is it appropriate to evaluate RKW theory in varying thermodynamic environments, but it is necessary to do so in order to determine the true merit of the vorticity balance framework.

In view of results presented above, we are inclined to believe that previous investigations supporting RKW theory (e.g., RKW88; Weisman et al. 1988; WR04; BKP06) did not control for latent heating by holding the

thermodynamic sounding fixed among different simulations. This possibility is consistent with the Lagrangian particle analysis of Weisman (1992), showing that parcels ascending within the deep convective line experienced more latent heating in cases having $\bar{c}/\Delta U$ closer to 1. And while we do not entirely dismiss the possibility of cold pool–shear balance effects being aliased into layer-lifting indices, especially because SLIF and $\Delta U/\bar{c}$ are strongly correlated (Pearson correlation coefficient of 0.89), we find support for the layer-lifting interpretation in the following observations:

- 1) Evidence that deep convection in SLs occurs as a layer-lifting process, both from observations (Zipser 1977; Kingsmill and Houze 1999; Evans and Doswell 2001; Gale et al. 2002; Coniglio et al. 2004; Cohen et al. 2007) and numerical experiments (Bryan and Fritsch 2000; Mechem et al. 2002; AK).
- 2) The tight clustering of points around a curve in Fig. 9b, suggesting a functional relationship between CAPE_{II} and \bar{B} , as well as the large diagnostic skill of w_{II} .
- 3) For each ΔU considered herein, simulations in DEEP environments produce more latent heating than those in SHALLOW (see \bar{B} in Table 2), the latter corresponding to more cold pool–shear balanced storms than the former (see Table 3), while both have identical near-surface CAPE (see Fig. 4). This behavior, which is largely accounted for by CAPE_{II} , does not support the contention of Weisman (1992) that, for a given near-surface CAPE, more cold pool–shear balanced storms produce greater latent heating owing to less updraft dilution (e.g., see AK).
- 4) $\bar{c}/\Delta U$ does not improve on ΔU as a diagnostic for features that RKW theory supposedly explains.

These considerations are of primary importance for interpreting the physical mechanisms through which shear affects the intensity of mature SLs, as exemplified by the linear regression analysis in section 4b (see Fig. 11), showing that, after controlling for latent heating, only 0.1 of the variance in w_{\max} is explained by $\Delta U/\bar{c}$. However, we acknowledge that more work is needed to make a precise attribution of the relative impacts of latent heating and vorticity balance on the intensity of mature SLs.

6. Conclusions

We analyzed numerical simulations of idealized SLs in various environmental settings, contemplating different strength of the low-tropospheric shear and varying cold pool intensities. Our results confirm

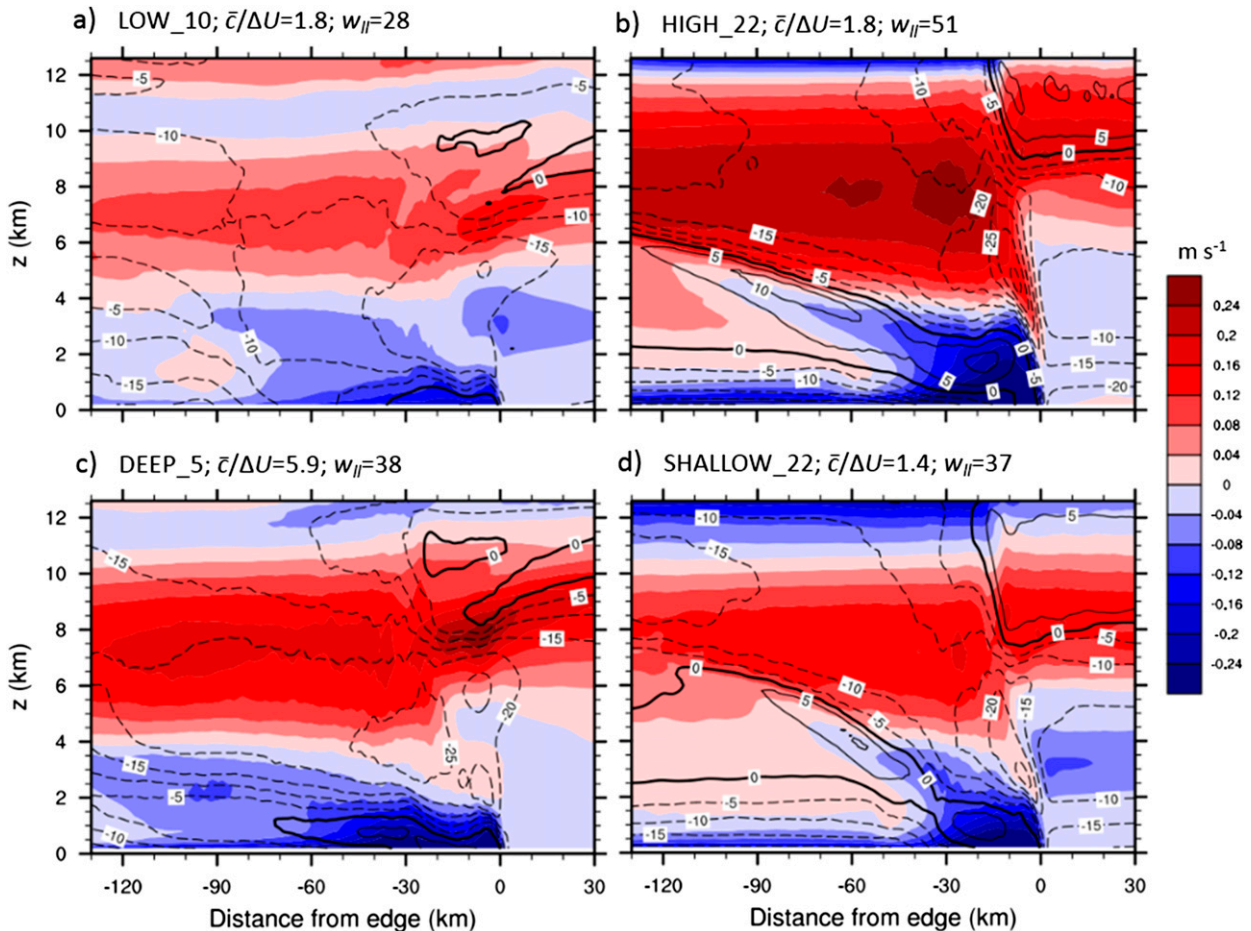


FIG. 15. Contour plots of along-line-averaged buoyancy (m s^{-2}) colored according to the label bar, with contours of along-line-averaged horizontal velocity overlaid at 5 m s^{-1} intervals (negative values are dashed). Plots correspond to (a) LOW_10, (b) HIGH_22, (c) DEEP_5, and (d) SHALLOW_22.

findings of AK (e.g., larger ICAPE tends to produce stronger cold pools), the PR is strongly dependent on the water vapor inflow rate, and greater mean convective instability of the inflowing air leads to larger within-storm buoyancy. These results constitute the basis for defining layer-lifting indices contemplating system-relative fluxes of relevant parameters, a framework referred to as the layer-lifting model of convection (LLMC). Layer-lifting indices can explain much of the intercase variability in updraft structure (e.g., 84% of the intercase variance of maximum vertical velocities), leading us to conclude that deep convective motions in mature SLs are primarily determined by the latent heating under the LLMC. The environmental shear at low levels plays a fundamental role by modulating the mean characteristics of the inflowing air, both in terms of water vapor and convective instability, while also affecting updraft verticality via the storm-relative inflow aloft. This

interpretation is consistent with observational evidence and results from previous numerical studies.

Our analyses indicate that cold pool-shear balance by itself might not represent as strong a constraint on the structure of mature SLs as previous investigations suggest. The well-known systematic dependence of mature SL intensity on the strength of the low-tropospheric shear, for a given thermodynamic sounding, is largely attributed to an underlying relationship between the shear's strength and the inflow of convectively unstable air as a fraction of the total storm-relative inflow. This interpretation is supported by the diagnostic skill of layer-lifting indices, together with results showing that, among the cases under consideration, SLs in more strongly sheared environments tend to produce greater mean convective instability of the storm-relative inflowing air. We also find that several metrics of SL intensity are better diagnosed by the strength of the low-tropospheric shear alone than by cold pool-shear balance. This is attributed to the fact that, within the

cold pool–dominated storms studied herein, the strongest SLs produce the most intense cold pools, the latter being inversely related to system optimality as conceived by RKW theory. Such behavior could explain the lack of observational support for the applicability of RKW theory to SLs (e.g., SCDE05).

More work is needed to make a precise attribution of latent heating under the LLMC and vorticity balance effects on the structure of SLs, including analyses focusing on the initial stages of storm development. It is important to highlight that our simulations do not span the full spectrum of environments in which SLs manifest. For instance, stronger cold pools are produced in environments with greater convective instability among simulations considered herein, which might not hold in general. Future studies should contemplate variations in the environmental temperature profile, more diverse kinematic settings (e.g., deeper shear), tropical environments, as well as investigations of layer lifting in other forms of organized convection. Ongoing research focuses on latent heating in SLs during the formative stages, as well as the modulation of the cold pool intensity by ICAPE, which contrasts with the commonly held notion that drier midtropospheric environments lead to stronger cold pools.

Acknowledgments. This paper benefited from reviews by Bradford S. Barrett, Editor Robert G. Fovell, and three anonymous reviewers. The author thanks George H. Bryan for making CM1 available. This study was partially funded by DGAPAUNAM postdoctoral fellowship and the PAPIIT program at UNAM under Grant IN104416. The author acknowledges computational resources of DGTICUNAM at Mitzli and the high-performance computing support from Yellowstone (ark:/85065/d7wd3xhc) provided by NCAR's Computational and Information Systems Laboratory, sponsored by the National Science Foundation.

REFERENCES

- Alfaro, D. A., and M. Khairoutdinov, 2015: Thermodynamic constraints on the morphology of simulated midlatitude squall lines. *J. Atmos. Sci.*, **72**, 3116–3137, doi:[10.1175/JAS-D-14-0295.1](https://doi.org/10.1175/JAS-D-14-0295.1).
- Bluestein, H. B., and M. H. Jain, 1985: Formation of mesoscale lines of precipitation: Severe squall lines in Oklahoma during the spring. *J. Atmos. Sci.*, **42**, 1711–1732, doi:[10.1175/1520-0469\(1985\)042<1711:FOMLOP>2.0.CO;2](https://doi.org/10.1175/1520-0469(1985)042<1711:FOMLOP>2.0.CO;2).
- Bryan, G. H., and J. M. Fritsch, 2000: Moist absolute instability: The sixth static stability state. *Bull. Amer. Meteor. Soc.*, **81**, 1207–1230, doi:[10.1175/1520-0477\(2000\)081<1287:MAITSS>2.3.CO;2](https://doi.org/10.1175/1520-0477(2000)081<1287:MAITSS>2.3.CO;2).
- , and —, 2002: A benchmark simulation for moist nonhydrostatic numerical models. *Mon. Wea. Rev.*, **130**, 2917–2928, doi:[10.1175/1520-0493\(2002\)130<2917:ABSFMN>2.0.CO;2](https://doi.org/10.1175/1520-0493(2002)130<2917:ABSFMN>2.0.CO;2).
- , and H. Morrison, 2012: Sensitivity of a simulated squall line to horizontal resolution and parameterization of microphysics. *Mon. Wea. Rev.*, **140**, 202–225, doi:[10.1175/MWR-D-11-00046.1](https://doi.org/10.1175/MWR-D-11-00046.1).
- , and R. Rotunno, 2014: The optimal state for gravity currents in shear. *J. Atmos. Sci.*, **71**, 448–468, doi:[10.1175/JAS-D-13-0156.1](https://doi.org/10.1175/JAS-D-13-0156.1).
- , J. C. Wyngaard, and J. M. Fritsch, 2003: Resolution requirements for the simulation of deep moist convection. *Mon. Wea. Rev.*, **131**, 2394–2416, doi:[10.1175/1520-0493\(2003\)131<2394:RRFTSO>2.0.CO;2](https://doi.org/10.1175/1520-0493(2003)131<2394:RRFTSO>2.0.CO;2).
- , D. Ahijevych, C. Davis, S. Trier, and M. Weisman, 2005: Observations of cold pool properties in mesoscale convective systems during BAMEX. Preprints, *11th Conf. on Mesoscale Processes*, Albuquerque, NM, Amer. Meteor. Soc., JP5J.12. [Available online at https://ams.confex.com/ams/32Rad11Meso/techprogram/paper_96718.htm.]
- , J. C. Knievel, and M. D. Parker, 2006: A multimodel assessment of RKW theory's relevance to squall-line characteristics. *Mon. Wea. Rev.*, **134**, 2772–2792, doi:[10.1175/MWR3226.1](https://doi.org/10.1175/MWR3226.1).
- Cohen, A. E., M. C. Coniglio, S. F. Corfidi, and S. J. Corfidi, 2007: Discrimination of mesoscale convective system environments using sounding observations. *Wea. Forecasting*, **22**, 1045–1062, doi:[10.1175/WAF1040.1](https://doi.org/10.1175/WAF1040.1).
- Coniglio, M. C., D. J. Stensrud, and M. B. Richman, 2004: An observational study of derecho-producing convective systems. *Wea. Forecasting*, **19**, 320–337, doi:[10.1175/1520-0434\(2004\)019<0320:AOSODC>2.0.CO;2](https://doi.org/10.1175/1520-0434(2004)019<0320:AOSODC>2.0.CO;2).
- , —, and L. J. Wicker, 2006: Effects of upper-level shear on the structure and maintenance of strong quasi-linear mesoscale convective systems. *J. Atmos. Sci.*, **63**, 1231–1252, doi:[10.1175/JAS3681.1](https://doi.org/10.1175/JAS3681.1).
- , S. F. Corfidi, and J. S. Kain, 2012: Views on applying RKW theory: An illustration using the 8 May 2009 derecho-producing convective system. *Mon. Wea. Rev.*, **140**, 1023–1043, doi:[10.1175/MWR-D-11-00026.1](https://doi.org/10.1175/MWR-D-11-00026.1).
- Deardorff, J. W., 1980: Stratocumulus-capped mixed layer derived from a three-dimensional model. *Bound.-Layer Meteor.*, **18**, 495–527, doi:[10.1007/BF00119502](https://doi.org/10.1007/BF00119502).
- Evans, J. S., and C. A. Doswell III, 2001: Examination of derecho environments using proximity soundings. *Wea. Forecasting*, **16**, 329–342, doi:[10.1175/1520-0434\(2001\)016<0329:EODEUP>2.0.CO;2](https://doi.org/10.1175/1520-0434(2001)016<0329:EODEUP>2.0.CO;2).
- Fovell, R. G., and Y. Ogura, 1989: Effect of vertical wind shear on numerically simulated multicell storm structure. *J. Atmos. Sci.*, **46**, 3144–3176, doi:[10.1175/1520-0469\(1989\)046<3144:EOVWSO>2.0.CO;2](https://doi.org/10.1175/1520-0469(1989)046<3144:EOVWSO>2.0.CO;2).
- , and P. S. Dailey, 1995: The temporal behavior of numerically simulated multicell-type storms. Part I. Modes of behavior. *J. Atmos. Sci.*, **52**, 2073–2095, doi:[10.1175/1520-0469\(1995\)052<2073:TTBONS>2.0.CO;2](https://doi.org/10.1175/1520-0469(1995)052<2073:TTBONS>2.0.CO;2).
- , and P. H. Tan, 1998: The temporal behavior of numerically simulated multicell-type storms. Part II: The convective cell life cycle and cell regeneration. *Mon. Wea. Rev.*, **126**, 551–577, doi:[10.1175/1520-0493\(1998\)126<0551:TTBONS>2.0.CO;2](https://doi.org/10.1175/1520-0493(1998)126<0551:TTBONS>2.0.CO;2).
- Gale, J. J., W. A. Gallus, and K. A. Jungbluth, 2002: Toward improved prediction of mesoscale convective system dissipation. *Wea. Forecasting*, **17**, 856–872, doi:[10.1175/1520-0434\(2002\)017<0856:TIPOMC>2.0.CO;2](https://doi.org/10.1175/1520-0434(2002)017<0856:TIPOMC>2.0.CO;2).
- Hane, C. E., 1973: The squall line thunderstorm: Numerical experimentation. *J. Atmos. Sci.*, **30**, 1672–1690, doi:[10.1175/1520-0469\(1973\)030<1672:TSLTNE>2.0.CO;2](https://doi.org/10.1175/1520-0469(1973)030<1672:TSLTNE>2.0.CO;2).

- James, R. P., J. M. Fritsch, and P. M. Markowski, 2005: Environmental distinctions between cellular and slabular convective lines. *Mon. Wea. Rev.*, **133**, 2669–2691, doi:[10.1175/MWR3002.1](https://doi.org/10.1175/MWR3002.1).
- Kingsmill, D. E., and R. A. Houze, 1999: Kinematic characteristics of air flowing into and out of precipitating convection over the west Pacific warm pool: An airborne Doppler radar survey. *Quart. J. Roy. Meteor. Soc.*, **125**, 1165–1207, doi:[10.1002/qj.1999.49712555605](https://doi.org/10.1002/qj.1999.49712555605).
- Lafore, J.-P., and M. W. Moncrieff, 1989: A numerical investigation of the organization and interaction of the convective and stratiform regions of tropical squall lines. *J. Atmos. Sci.*, **46**, 521–544, doi:[10.1175/1520-0469\(1989\)046<0521:ANIOTO>2.0.CO;2](https://doi.org/10.1175/1520-0469(1989)046<0521:ANIOTO>2.0.CO;2).
- Lebo, Z. J., and H. Morrison, 2015: Effects of horizontal and vertical grid spacing on mixing in simulated squall lines and implications for convective strength and structure. *Mon. Wea. Rev.*, **143**, 4355–4375, doi:[10.1175/MWR-D-15-0154.1](https://doi.org/10.1175/MWR-D-15-0154.1).
- LeMone, M. A., E. J. Zipser, and S. B. Trier, 1998: The role of environmental shear and thermodynamic conditions in determining the structure and evolution of mesoscale convective systems during TOGA COARE. *J. Atmos. Sci.*, **55**, 3493–3518, doi:[10.1175/1520-0469\(1998\)055<3493:TROESA>2.0.CO;2](https://doi.org/10.1175/1520-0469(1998)055<3493:TROESA>2.0.CO;2).
- Liu, C., and M. W. Moncrieff, 1996: An analytical study of density currents in sheared, stratified fluids including the effects of latent heating. *J. Atmos. Sci.*, **53**, 3303–3312, doi:[10.1175/1520-0469\(1996\)053<3303:AASODC>2.0.CO;2](https://doi.org/10.1175/1520-0469(1996)053<3303:AASODC>2.0.CO;2).
- Mechem, D. B., R. A. Houze, and S. S. Chen, 2002: Layer inflow into precipitating convection over the western tropical Pacific. *Quart. J. Roy. Meteor. Soc.*, **128**, 1997–2030, doi:[10.1256/003590002320603502](https://doi.org/10.1256/003590002320603502).
- Moncrieff, M. W., and C. Liu, 1999: Convection initiation by density currents: Role of convergence, shear, and dynamical organization. *Mon. Wea. Rev.*, **127**, 2455–2464, doi:[10.1175/1520-0493\(1999\)127<2455:CIBDCR>2.0.CO;2](https://doi.org/10.1175/1520-0493(1999)127<2455:CIBDCR>2.0.CO;2).
- Morrison, H., J. A. Curry, and V. I. Khvorostyanov, 2005: A new double-moment microphysics parameterization for application in cloud and climate models. Part I: Description. *J. Atmos. Sci.*, **62**, 1678–1693, doi:[10.1175/JAS3447.1](https://doi.org/10.1175/JAS3447.1).
- , S. A. Tessendorf, K. Ikeda, and G. Thompson, 2012: Sensitivity of a simulated midlatitude squall line to parameterization of raindrop breakup. *Mon. Wea. Rev.*, **140**, 2437–2460, doi:[10.1175/MWR-D-11-00283.1](https://doi.org/10.1175/MWR-D-11-00283.1).
- , J. A. Milbrandt, G. H. Bryan, K. Ikeda, S. A. Tessendorf, and G. Thompson, 2015: Parameterization of cloud microphysics based on the prediction of bulk ice particle properties. Part 2: Case study comparisons with observations and other schemes. *J. Atmos. Sci.*, **72**, 312–339, doi:[10.1175/JAS-D-14-0066.1](https://doi.org/10.1175/JAS-D-14-0066.1).
- Newton, C. W., 1950: Structure and mechanism of the prefrontal squall line. *J. Meteor.*, **7**, 210–222, doi:[10.1175/1520-0469\(1950\)007<0210:SAMOTP>2.0.CO;2](https://doi.org/10.1175/1520-0469(1950)007<0210:SAMOTP>2.0.CO;2).
- Nicholls, M. E., R. H. Johnson, and W. R. Cotton, 1988: The sensitivity of two-dimensional simulations of tropical squall lines to environmental profiles. *J. Atmos. Sci.*, **45**, 3625–3649, doi:[10.1175/1520-0469\(1988\)045<3625:TSOTDS>2.0.CO;2](https://doi.org/10.1175/1520-0469(1988)045<3625:TSOTDS>2.0.CO;2).
- Pandya, R. E., and D. R. Durran, 1996: The influence of convectively generated thermal forcing on the mesoscale circulation around squall lines. *J. Atmos. Sci.*, **53**, 2924–2951, doi:[10.1175/1520-0469\(1996\)053<2924:TIOCGT>2.0.CO;2](https://doi.org/10.1175/1520-0469(1996)053<2924:TIOCGT>2.0.CO;2).
- Parker, M. D., 2010: Relationship between system slope and updraft intensity in squall lines. *Mon. Wea. Rev.*, **138**, 3572–3578, doi:[10.1175/2010MWR3441.1](https://doi.org/10.1175/2010MWR3441.1).
- , and R. H. Johnson, 2000: Organizational modes of mid-latitude mesoscale convective systems. *Mon. Wea. Rev.*, **128**, 3413–3436, doi:[10.1175/1520-0493\(2001\)129<3413:OMOMMC>2.0.CO;2](https://doi.org/10.1175/1520-0493(2001)129<3413:OMOMMC>2.0.CO;2).
- , and —, 2004: Structures and dynamics of quasi-2D mesoscale convective systems. *J. Atmos. Sci.*, **61**, 545–567, doi:[10.1175/1520-0469\(2004\)061<0545:SADOQM>2.0.CO;2](https://doi.org/10.1175/1520-0469(2004)061<0545:SADOQM>2.0.CO;2).
- Rickenbach, T. M., and S. A. Rutledge, 1998: Convection in TOGA COARE: Horizontal scale, morphology, and rainfall production. *J. Atmos. Sci.*, **55**, 2715–2729, doi:[10.1175/1520-0469\(1998\)055<2715:CITCHS>2.0.CO;2](https://doi.org/10.1175/1520-0469(1998)055<2715:CITCHS>2.0.CO;2).
- Rotunno, R., J. B. Klemp, and M. L. Weisman, 1988: A theory for strong, long-lived squall lines. *J. Atmos. Sci.*, **45**, 463–485, doi:[10.1175/1520-0469\(1988\)045<0463:ATFSL>2.0.CO;2](https://doi.org/10.1175/1520-0469(1988)045<0463:ATFSL>2.0.CO;2).
- , —, and —, 1990: Comments on “A numerical investigation of the organization and interaction of the convective and stratiform regions of tropical squall lines.” *J. Atmos. Sci.*, **47**, 1031–1033, doi:[10.1175/1520-0469\(1990\)047<1031:CONIOT>2.0.CO;2](https://doi.org/10.1175/1520-0469(1990)047<1031:CONIOT>2.0.CO;2).
- Shapiro, A., 1992: A hydrodynamical model of shear flow over semi-infinite barriers with application to density currents. *J. Atmos. Sci.*, **49**, 2293–2305, doi:[10.1175/1520-0469\(1992\)049<2293:AHMOSF>2.0.CO;2](https://doi.org/10.1175/1520-0469(1992)049<2293:AHMOSF>2.0.CO;2).
- Stensrud, D. J., M. C. Coniglio, R. P. Davies-Jones, and J. S. Evans, 2005: Comments on “A theory for strong long-lived squall lines” revisited. *J. Atmos. Sci.*, **62**, 2989–2996, doi:[10.1175/JAS3514.1](https://doi.org/10.1175/JAS3514.1).
- Thorpe, A. J., M. J. Miller, and M. W. Moncrieff, 1982: Two-dimensional convection in non-constant shear: A model of mid-latitude squall lines. *Quart. J. Roy. Meteor. Soc.*, **108**, 739–762, doi:[10.1002/qj.49710845802](https://doi.org/10.1002/qj.49710845802).
- von Kármán, T., 1940: The engineer grapples with nonlinear problems. *Bull. Amer. Math. Soc.*, **46**, 615–683, doi:[10.1090/S0002-9904-1940-07266-0](https://doi.org/10.1090/S0002-9904-1940-07266-0).
- Weisman, M. L., 1992: The role of convectively generated rear-inflow jets in the evolution of long-lived mesoconvective systems. *J. Atmos. Sci.*, **49**, 1826–1847, doi:[10.1175/1520-0469\(1992\)049<1826:TROCGR>2.0.CO;2](https://doi.org/10.1175/1520-0469(1992)049<1826:TROCGR>2.0.CO;2).
- , and J. B. Klemp, 1982: The dependence of numerically simulated convective storms on vertical wind shear and buoyancy. *Mon. Wea. Rev.*, **110**, 504–520, doi:[10.1175/1520-0493\(1982\)110<0504:TDONSC>2.0.CO;2](https://doi.org/10.1175/1520-0493(1982)110<0504:TDONSC>2.0.CO;2).
- , and R. Rotunno, 2004: “A theory for strong long-lived squall lines” revisited. *J. Atmos. Sci.*, **61**, 361–382, doi:[10.1175/1520-0469\(2004\)061<0361:ATFSLS>2.0.CO;2](https://doi.org/10.1175/1520-0469(2004)061<0361:ATFSLS>2.0.CO;2).
- , J. B. Klemp, and R. Rotunno, 1988: Structure and evolution of numerically simulated squall lines. *J. Atmos. Sci.*, **45**, 1990–2013, doi:[10.1175/1520-0469\(1988\)045<1990:SAEONS>2.0.CO;2](https://doi.org/10.1175/1520-0469(1988)045<1990:SAEONS>2.0.CO;2).
- Zipser, E. J., 1977: Mesoscale and convective-scale downdrafts as distinct components of squall-line structure. *Mon. Wea. Rev.*, **105**, 1568–1589, doi:[10.1175/1520-0493\(1977\)105<1568:MACDAD>2.0.CO;2](https://doi.org/10.1175/1520-0493(1977)105<1568:MACDAD>2.0.CO;2).